Journal of the Indian Chemical Society 103 (2026) 102386

Contents lists available at ScienceDirect

Journal of the Indian Chemical Society

journal homepage: www.journals.elsevier.com/journal-of-the-indian-chemical-society

Tunable Copper-doped $BaZrO_3$ for generation of hydrogen through photocatalytic water splitting

Catalina Vega-Reyes [a], Iliana E. Medina-Ramírez [b], Luis A. Díaz-Torres [c], Eduardo Coutiño-González [d], Patricia M. Olmos-Moya [e], Carlos A. Pineda-Arellano [f,*]

[a] Posgrado Interinstitucional de Ciencia y Tecnología – Centro de Investigaciones en Óptica A.C. – Unidad Aguascalientes, Calle Prol. Constitución 607, Fraccionamiento Reserva Loma Bonita, C.P. 20200, Aguascalientes, Ags., Mexico
[b] Universidad Autónoma de Aguascalientes, Av. Universidad 940, Ciudad Universitaria, C.P. 20100, Aguascalientes, Ags., Mexico
[c] Laboratorio de Fotocatálisis y Fotosíntesis Artificial (F&FA), Centro de Investigaciones en Óptica A.C., Loma del Bosque 115, Lomas del Campestre, C.P. 37150, León de los Aldama, Gto., Mexico
[d] Interuniversity Microelectronics Center (imec), Remisebosweg 1, 3001, Leuven, Belgium
[e] División de Ciencias e Ingeniería, Universidad de Guanajuato, Lomas del Bosque #103, Lomas del Campestre, C.P. 37150, León, Gto., Mexico
[f] SECIHTI – Centro de Investigaciones en Óptica A.C., Prol. Constitución 607, Fracc. Reserva Loma Bonita, C.P. 20200, Aguascalientes, Ags., Mexico

ARTICLE INFO

Keywords:
$BaZrO_3$
Photocatalytic hydrogen
Perovskite material
Water splitting

ABSTRACT

$BaZrO_3$, a perovskite-type semiconductor, exhibits exceptional stability and tunable electronic properties, making it a promising candidate for photocatalytic applications. In this study, Cu-doped $BaZrO_3$ was synthesized by a hydrothermal method followed by thermal annealing at 1100 °C. The substitution of Cu within the $BaZrO_3$ lattice improves H_2 evolution efficiency. It enhances photosensitivity by introducing electronic defects, increasing the photogenerated electron lifetime (19.89 ns), increasing the specific surface area (19.35 m^2/g), and narrowing the band gap (3.4 eV) of calcined $BaZrO_3$ containing 0.5 % Cu. The X-ray Photoelectron Spectroscopy study showed that Cu^+/Cu^{2+} was effectively incorporated into the $BaZrO_3$ structure by substituting for Zr^{3+}/Zr^{4+}, creating O vacancies, and thereby improving the optical performance of the doped materials. The materials exhibit photosensitivity that decreases with the highest Cu doping. However, the most beneficial H_2 evolution by photocatalysis occurs at an impurity level is 0.5 % Cu. The importance of the calcination treatment was evident, as it reduces the presence of unwanted species such as $BaCO_3$. Inductively Coupled Plasma studies confirmed a good approximation of the expected Cu concentrations. Photocatalysis results showed the best hydrogen production (27.2 μmol g^{-1} h^{-1} and apparent quantum yield = 0.54 %) when $BaZrO_3$ was doped with 0.5 at% copper.

1. Introduction

Access to sustainable and reliable energy is essential for economic development and improving the quality of life, particularly in emerging economies. However, the global reliance on fossil fuels significantly contributes to environmental degradation and climate change, underscoring the urgency of developing cleaner energy alternatives [1]. Solar energy, among renewable sources, stands out for its abundance and renewability, yet its intermittent nature poses challenges for consistent supply and storage. Hydrogen has attracted considerable interest as a clean energy vector and an efficient energy storage medium, even though more than 96 % of global hydrogen production currently comes from fossil fuels [2]. Photocatalytic water splitting offers a sustainable pathway to hydrogen generation using only sunlight and water as inputs [3]. Hydrogen can store energy in its chemical bonds [4], making it one of the most promising solutions for overcoming the intermittency of renewable energy sources and enhancing grid stability [5,6]. However, its large-scale production faces limitations, primarily due to low quantum efficiency caused by rapid recombination of photogenerated charge carriers and catalyst degradation [7]. Addressing these challenges requires the development of semiconductors and co-catalysts based on earth-abundant elements to improve charge separation, light absorption, and overall photocatalytic performance [8,9]. Photocatalytic water splitting on semiconductor surfaces involves photon absorption, the generation of electron–hole pairs, and subsequent redox reactions in water [10]. Electrons reduce protons to form hydrogen gas, while holes

* Corresponding author.
E-mail address: capia@cio.mx (C.A. Pineda-Arellano).

https://doi.org/10.1016/j.jics.2025.102386
Received 5 August 2025; Received in revised form 11 December 2025; Accepted 28 December 2025
Available online 29 December 2025

oxidize water to generate oxygen [11]. Effective separation and transport of these charge carriers are critical to avoid recombination and ensure high hydrogen production efficiency [12]. Different materials have been investigated for photocatalytic hydrogen production, including TiO_2, MoS_2, CdS, SiC, and g-C_3N_4 [13]. One of the knowledge gaps in photocatalytic water-splitting technology is to eliminate or reduce the use of precious metals, expensive materials, or complex materials. Among these, perovskite-type oxides have emerged as particularly promising due to their structural versatility, chemical stability, and tunable electronic properties [14]. Barium zirconate ($BaZrO_3$), a cubic perovskite ($Pm\bar{3}m$ space group), offers high thermal stability (melting point ~2700 °C), low thermal expansion, and excellent chemical resistance [15,16]. Its general structure (ABO_3) allows for extensive doping, enabling modulation of its electrical, optical, and catalytic properties [17]. In this context, perovskite-type oxides (ABO_3) have emerged as a highly attractive class of materials due to their structural versatility, chemical stability, and electronically tunable properties via doping [18]. The wide band gap and mechanical robustness of $BaZrO_3$, along with its suitability for doping at the A (Ba^{2+}) or B (Zr^{4+}) sites, make it a strong candidate for photochemical applications [17,19]. Recent studies also indicate that the synergy between metal doping and oxygen defects generates intermediate energy levels that broaden visible-light absorption and facilitate directional charge transport [20]. Yuan et al. reported that $BaZrO_3$ can drive water splitting in the absence of a cocatalyst [21]. Yttrium-doped $BaZrO_3$ has been widely investigated for applications in proton-conducting fuel cells, methane conversion, and electrolyzers [22]. Other dopants, such as cerium (Ce), have been used for pollutant degradation [23,24] and in proton ceramic fuel cells [25]. Additionally, $BaZrO_3$ has shown promise in photocatalytic hydrogen production [26,27], and co-doping strategies such as Y [22] or Ce [25] have been employed to improve proton conductivity by introducing oxygen vacancies. These modifications enhance charge transport and catalytic performance. Transition metal oxides are also commonly employed as synthesis adjuvants [28]. Z. Qiao et al. reported that Cu-doped $BaZrO_3$ synthesized via solid-state methods exhibited high resistance to thermal shock and mechanical stress, positioning it as a suitable material for demanding energy applications [29]. In the present work, the effect of the Cu atomic percentage in Cu-doped $BaZrO_3$ on photocatalytic hydrogen evolution activity is studied. Leveraging the intrinsic thermal and structural stability of $BaZrO_3$, its cubic structure ($Pm\bar{3}m$) [27], and its capacity to host dopants. This work explores how Cu incorporation modulates the band gap, induces oxygen vacancies, and enhances charge separation and light absorption. The goal is to evaluate hydrogen production efficiency under Hg light irradiation, advancing the development of cost-effective, sustainable photocatalysts for hydrogen generation.

2. Experimental

2.1. Chemicals and materials

All chemical reagents used in this study were of analytical grade and were used without further purification. The materials included zirconyl chloride octahydrate ($Cl_2OZr{\cdot}8H_2O$, 98%, Aldrich), hexadecyltrimethylammonium bromide (CTAB, 98%, Aldrich), barium nitrate ($Ba(NO_3)_2$, 99%, Aldrich), and sodium hydroxide (NaOH, 98%, J.T. Baker). Copper (II) nitrate trihydrate ($Cu(NO_3)_2{\cdot}3H_2O$, Aldrich) was used as the doping agent. Deionized water, obtained from an Arium® Mini ultrapure water system with a conductivity of 0.055 μS/cm, and analytical-grade ethanol and acetone (Baker Analyzed absolute mass) were used as solvents. All reagents were handled under controlled laboratory conditions to ensure reproducibility and precision in the synthesis process.

2.2. Synthesis of copper-doped $BaZrO_3$

The Cu-doped $BaZrO_3$ photocatalysts were synthesized via the hydrothermal method with Cu doping atomic ratios of 0.5, 1.0, 2.5, and 5.0 at% with respect to Zr atoms. The synthesis process began with the preparation of a precursor solution by dissolving $Ba(NO_3)_2$ (source of Ba^{2+}, corresponding to the A-site cation in the perovskite structure), $Cl_2OZr{\cdot}8H_2O$ (source of Zr^{4+}, the B-site cation), and $Cu(NO_3)_2{\cdot}3H_2O$ (Cu^{2+} dopant source) in 100 mL of deionized water, which acts as a dissolution medium and provides the hydrothermal environment necessary for controlled crystallization. The mixture was stirred in a 1000 mL KIMAX® vessel for 30 min to ensure complete homogenization. Subsequently, 100 mL of ethanol was added as a co-solvent, used to reduce surface tension and improve dispersion by modifying the polarity of the reaction medium. A measured amount of CTAB was then incorporated to function as a cationic surfactant. CTAB adsorbs onto the surface of crystal nuclei during synthesis, modulating anisotropic crystal growth. This interaction promotes the formation of well-defined morphologies such as extended dodecahedrons in $BaZrO_3$ and suppresses uncontrolled particle agglomeration and growth [30]. NaOH was subsequently added to adjust the pH and promote precipitation of the metal hydroxide intermediates, thereby favoring nucleation. The resulting mixture was stirred vigorously for 60 min and ultrasonicated in a water bath at 30 °C for 20 min to enhance homogeneity and dispersion. The suspension was then transferred to a Teflon-lined stainless-steel autoclave and subjected to hydrothermal treatment at 100 °C for 24 h to promote crystallization. The precipitated material was recovered by centrifugation and washed sequentially with acetone, deionized water, ethanol, and deionized water to remove organic and ionic impurities. The washed material was dried at 100 °C for 15 h, then at 120 °C to ensure complete moisture removal. Finally, the dried powder was ground using an agate mortar and calcined in a muffle furnace at 1100 °C for 3 h to enhance crystallinity and reach complete phase formation. The pristine and uncalcined sample is designated as UC-$BaZrO_3$, while the uncalcined and doped samples are labeled as UC-$BaZrO_3$:Cu (0.5 %), UC-$BaZrO_3$:Cu(1.0 %), UC-$BaZrO_3$:Cu(2.5 %), and UC $BaZrO_3$Cu(5.0 %). Similarly, the pristine and calcined sample is identified as C–$BaZrO_3$, whereas the calcined and doped samples are referred to as C–$BaZrO_3$:Cu(0.5 %), C–$BaZrO_3$:Cu(1.0 %), C–$BaZrO_3$:Cu(2.5 %), and C-$BaZrO_3$:Cu(5.0 %).

2.3. Characterization

The $BaZrO_3$ and Cu-doped $BaZrO_3$ photocatalysts (0.5, 1.0, 2.5, and 5.0 at%) were characterized by X-ray diffraction (XRD, Bruker D2 PHASER) to analyze the crystalline structure. The XRD measurements were performed with a step size of 0.0203° in θ and a scanning range of 10°-70° in 2θ , using Cu Kα radiation (λ = 1.54184 Å). Scanning electron microscopy (SEM, JEOL JSM-7800 F) provided insights into morphology and particle size. UV–Vis diffuse reflectance spectroscopy was performed on a Thermo Scientific™ Evolution 201/220 spectrophotometer, measuring the absorbance. Fourier transform infrared spectroscopy (FTIR) was performed on an Agilent Cary 670 coupled with a Cary 620 to identify functional groups and bonding. The specific BET area and pore size were evaluated using an Autosorb iQ AG instrument with the BET and BJH equations, respectively. Inductively Coupled Plasma Optical Emission Spectroscopy (ICP-OES) measurements were carried out using a Varian 730-ES spectrometer. X-ray Photoelectron Spectroscopy (XPS) analysis was performed on a Thermo Fisher Scientific® instrument equipped with a monochromatic Al $K\alpha_1$ X-ray source (photon energy = 1486.7 eV, Model XR5). The spectra were acquired over the binding-energy range of 0–1400 eV, employing a pass energy of 20.0 eV and an energy step size of 0.100 eV. Electrochemical characterization tests were conducted by using a conventional three-electrode system. A platinum mesh was used as the counter electrode, a saturated calomel electrode (SCE) as the reference electrode, and the working electrode

consisted of $BaZrO_3$ or Cu-doped $BaZrO_3$ films deposited onto FTO glass substrates via the screen-printing method. The measurements were carried out in a 0.1 M NaOH electrolyte under alkaline aqueous conditions (pH 13). Experiments were performed both in the dark and under illumination using a 75 W xenon lamp as the light source. All electrochemical tests were conducted using a BioLogic brand potentiostat/galvanostat. Hydrogen evolution was quantified using a Shimadzu GC-2014 gas chromatograph. The photocatalytic reaction was carried out in triplicate in a 200 mL cell containing deionized water and 0.05 g of the photocatalyst under irradiation from a Hg pen lamp (Pen-Ray, 254 nm).

3. Results

3.1. Crystalline phase analysis

Fig. 1 shows the X-ray diffraction patterns of calcined pristine and Cu-doped $BaZrO_3$ (0.5, 1.0, 2.5, and 5.0 at%) calcined materials. All samples exhibit diffraction peaks corresponding to a cubic perovskite structure, in agreement with the characteristic (1 1 0), (1 1 1), (2 0 0), (2 1 1), and (2 2 0) planes of $BaZrO_3$ according to card 00-153-8369 [31]. The crystalline structure is identified as cubic with space group $Pm\bar{3}m$.

The appearance of $BaCO_3$ (witherite) as a segregated phase in both pristine and Cu-doped $BaZrO_3$ uncalcined samples (Figures SM-1 and SM-2) is a well-documented phenomenon arising from multiple concurrent mechanisms involving solid-state reaction kinetics, carbonate thermodynamics, and dopant-induced surface chemistry. Even after calcination, traces of $BaCO_3$ can persist because its decomposition and reaction with ZrO_2 are diffusion-controlled and highly sensitive to treatment temperature and stoichiometry [27]. During the solid-state route, $BaCO_3$ reacts with ZrO_2 to form $BaZrO_3$ via interfacial diffusion; however, incomplete conversion often occurs when ion diffusion across the $BaZrO_3/ZrO_2$ interface is kinetically limited below ~1100 °C [32]. As a result, unreacted $BaCO_3$ cores remain embedded within the perovskite matrix and can be readily identified by their characteristic reflections at $2\theta \approx 24–28°$ in XRD patterns [28,29]. In addition to incomplete solid-state transformation, surface carbonation can regenerate $BaCO_3$ during cooling or post-synthesis exposure to ambient air. Density functional theory calculations show that CO_2 adsorption on $BaZrO_3$ (0 0 1) is exothermic and leads to spontaneous formation of stable surface carbonates at temperatures as low as 100 °C [30]. Experimental studies corroborate this behavior: $BaZrO_3$ ceramics exposed to CO_2 between 600 °C and 800 °C exhibit the development of $BaCO_3$ surface layers and concurrent Ba depletion in the underlying perovskite [31].

The presence and intensity of the $BaCO_3$ diffractions are more pronounced in samples doped with Cu at 1.0–5.0 at% (Fig. SM–1), suggesting that Cu incorporation influences both chemical homogeneity and surface reactivity. Dopant-induced defect formation and cation segregation are known to disturb local stoichiometry, promoting Ba-rich or Cu-rich domains that act as preferential sites for carbonate stabilization [33]. In $BaZrO_3$, dopants with limited solid solubility, such as Cu^{2+}, can exsolve during high-temperature treatment, forming nanometric Cu-rich clusters or secondary phases at grain boundaries [34]. This exsolution process alters the interfacial chemistry and increases the availability of Ba at exposed surfaces, thereby enhancing the likelihood of $BaCO_3$ formation upon contact with CO_2 [35]. As Cu concentration increases from 1.0 to 5.0 at%, the likelihood of local non-stoichiometric regions increases, explaining the progressive evolution of $BaCO_3$ signals in XRD from uncalcined samples.

Moreover, the partial substitution of Zr^{4+} by Cu^{2+} introduces lattice strain and charge-compensating defects (e.g., oxygen vacancies) [33], which can further facilitate Ba^{2+} migration toward the surface and subsequent carbonatation. From a functional standpoint, $BaCO_3$ is electrically insulating and non-photocatalytic; its presence decreases phase purity and can block active surface sites or scatter incident light, potentially compromising photocatalytic efficiency. To minimize its formation, it is crucial to employ prolonged calcination at ≥1100 °C and ensure precise stoichiometric control [27,31].

The calcined Cu-doped samples (Table 1) exhibit larger crystallite sizes than pristine $BaZrO_3$, suggesting that small amounts of Cu may act as crystallization facilitators during the early stages of synthesis. Comparative analysis of uncalcined and calcined samples shows that calcination is a crucial step for achieving a homogeneous and phase-pure perovskite in Cu-doped $BaZrO_3$ systems. The uncalcined samples (Table SM1 and Fig. 2) contain residual C-rich secondary phases, such as $BaCO_3$, which are eliminated during calcination. This indicates improved Cu diffusion and reaction kinetics within the crystalline lattice during thermal treatment. Furthermore, the structural data demonstrate that Cu incorporation alters unit cell parameters and increases defect density of the calcined samples, which can significantly influence the material's functional properties, such as photocatalytic activity and ionic conductivity [34]. More specifically, the lattice parameter “a" decreases progressively from 0.427 nm in pristine calcined $BaZrO_3$ to values ranging between 0.416 and 0.418 nm in Cu-doped samples, depending on the Cu concentration. This contraction is consistent with the

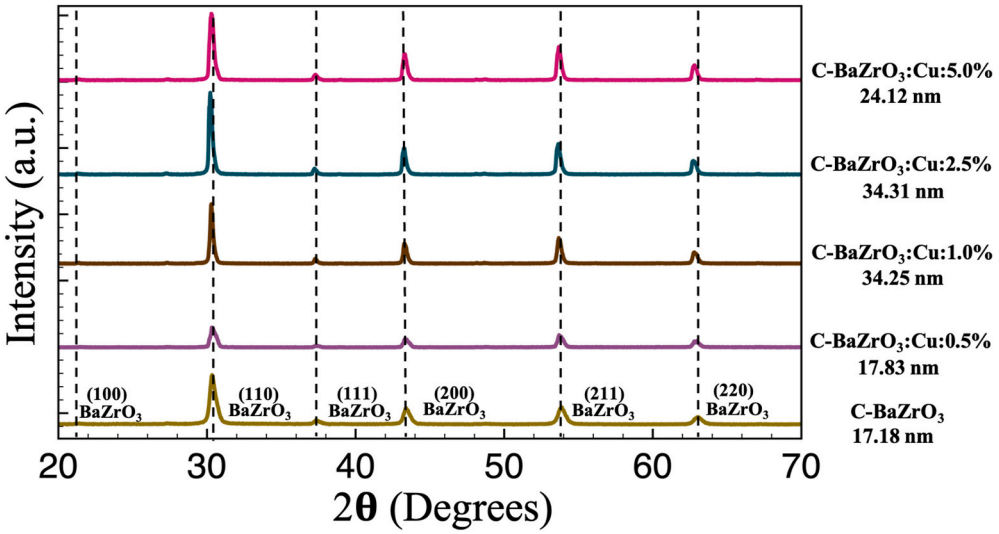

Fig. 1. X-ray diffraction patterns of calcined pristine and Cu-doped $BaZrO_3$ (0.5 %, 1.0 %, 2.5 %, 5.0 at%). The diffraction peaks correspond to the cubic perovskite $BaZrO_3$ (card [00-153-8369]). The average crystallite size, estimated using the Scherrer equation, is shown to the left of the figure.

Table 1
Structural parameter data obtained from X-ray diffraction patterns of pristine and Cu-doped (0.5 %, 1.0 %, 2.5 %, 5.0 at%) calcined $BaZrO_3$ (View Table SM–1 for uncalcined materials).

Sample	2θ (degrees)	Crystal size (nm)	Interplanar distance (d110) (nm)	Lattice parameter (a) (nm)	Cell volume (V) (nm^3)	Density (ρ) ($g{\cdot}cm^{-3}$)
C–$BaZrO_3$	29.56	17.18	0.302	0.427	0.077	5.894
C–$BaZrO_3$:Cu(0.5 %)	30.31	17.83	0.294	0.416	0.072	6.344
C–$BaZrO_3$:Cu(1.0 %)	30.29	34.25	0.294	0.417	0.072	6.331
C–$BaZrO_3$:Cu(2.5 %)	30.21	34.31	0.295	0.418	0.073	6.282
C–$BaZrO_3$:Cu(5.0 %)	30.29	24.12	0.294	0.417	0.072	6.331

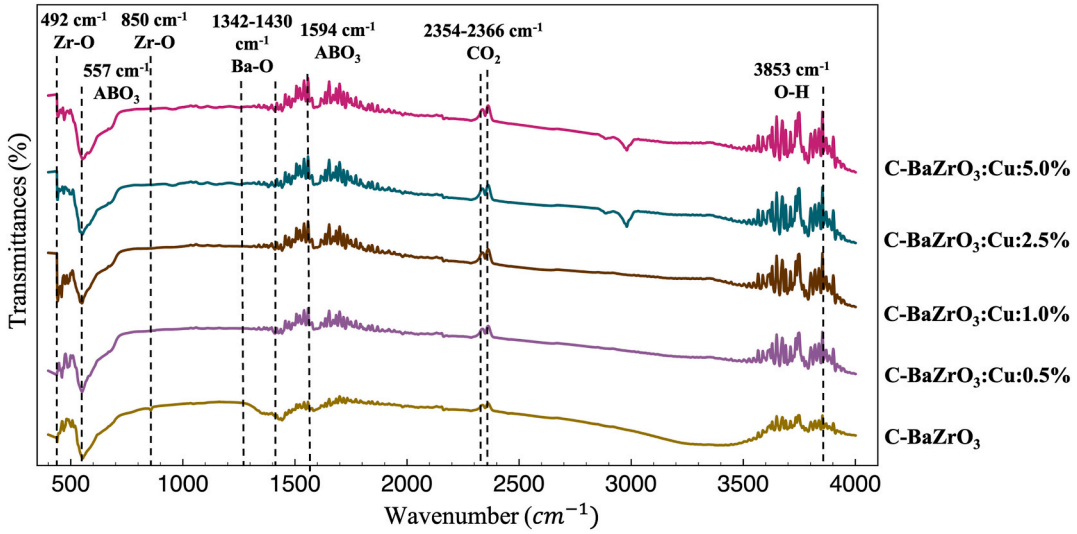

Fig. 2. FTIR spectrum of calcined pristine and Cu-doped $BaZrO_3$ perovskite (0.5, 1.0, 2.5, 5.0 at%).

incorporation of Cu^{2+} into the Zr^{4+} sites and the associated lattice distortion. Concurrently, crystallite size increases from 17.18 nm (pristine $BaZrO_3$) to 34.31 nm in the 2.5 at% Cu-doped calcined sample, suggesting that Cu may facilitate crystal growth, while introducing structural disorder [28].

3.2. Infrared spectroscopy

The functional groups were identified using Fourier transform infrared spectroscopy (FTIR), which provides vibrational-rotational spectra. Fig. SM–3 presents the FTIR spectra of uncalcined pristine and Cu-doped $BaZrO_3$ (0.5, 1.0, 2.5, and 5.0 at%). A vibrational band at 492 cm^{-1} corresponds to Zr–O stretching vibrations [35]. While the peak at 850 cm^{-1} is also attributed to Zr–O bonds [36]. Additionally, the vibrational mode at 1446 cm^{-1} is associated with Ba–O bonds [35], whereas the bands at 1550 cm^{-1} are linked to O–H stretching vibrations. In the 1.0, 2.5, and 5.0 at% Cu-doped samples, additional O–H bonds are detected at 2927 cm^{-1}, 3737 cm^{-1}, and 3890 cm^{-1}.

Fig. 2 shows the infrared spectra of calcined $BaZrO_3$ nanoparticles and Cu-doped $BaZrO_3$ (0.5, 1.0, 2.5, and 5.0 at%). The spectra exhibit similar patterns to those observed in the uncalcined samples. A vibrational band at 492 cm^{-1}, characteristic of Zr–O stretching vibrations, confirms the presence of metal–oxygen bonds [35]. Additionally, a vibrational band at 557 cm^{-1} is associated with metal-oxygen stretching vibrations, typical of the ABO_3 perovskite structure [37]. The peak at 850 cm^{-1} corresponds to asymmetric Zr–O stretching vibrations [38], while the cluster of peaks in the 1342–1430 cm^{-1} range is attributed to Ba–O vibrational modes within the sample [39]. A minor peak at 1594 cm^{-1} is linked to metal-oxygen stretching vibrations within the ABO_3 perovskite network [40]. The small peaks at 2354 cm^{-1} and 2366 cm^{-1} are likely due to atmospheric CO_2 absorption during the analysis [41]. Lastly, a low-intensity peak at 3853 cm^{-1} confirms the presence of O–H groups in the synthesized perovskites [35]. A strong band is observed in the region between ~450 and ~600 cm^{-1} for all samples, which mainly corresponds to the Zr–O stretching typical of the $BaZrO_3$ perovskite structure. The uncalcined samples exhibit characteristic bands associated with Zr–O (~492 and 850 cm^{-1}) and Ba–O (~1446 cm^{-1}) vibrations, along with intense O–H stretching modes (1550 cm^{-1} and in the 2927–3890 cm^{-1} region), which indicate the presence of surface adsorbed moisture, undecomposed precursors, and possibly carbonate species features typical of uncalcined precursors. In contrast, the calcined samples retain the main Zr–O and Ba–O vibrations but display a more defined spectral profile with significantly reduced O–H signals, reflecting improved structural purity and thermal decomposition of residual groups. Notably, in Cu-doped samples, particularly those with 2.5 % and 5.0 % Cu, an increase in intensity or broadening is observed in the 450–600 cm^{-1} region in both calcined and uncalcined specimens. This suggests the presence of Cu–O bonds that overlap with the Zr–O vibrational modes [42]. In summary, calcination enhances structural clarity and eliminates surface residues, while the Cu–O signal is observed under both conditions, indicating that Cu incorporation occurs as early as the synthesis stage.

3.3. Morphological and BET surface area

The Cu-doped $BaZrO_3$ samples (0.5, 1.0, 2.5, and 5.0 at%) exhibit a distinctive morphology characterized by elongated dodecahedra (see Figure SM-4 and Fig. 3), also referred to as extended rhombic dodecahedra. This morphology is strongly influenced by the hydrothermal synthesis method, which is well documented for promoting anisotropic crystal growth [43]. A similar structure has been reported in the literature, for example, in the study by K. Kanie et al. (2014), in which europium-doped $BaZrO_3$ synthesized via hydrothermal methods displayed comparable morphologies [44]. Similarly, ytterbium doping has shown analogous results [35]. This geometric configuration is commonly observed in 14-faced binary crystal structures, involving

individual cubic phase crystals with prominent facets such as [0 0 1] and [1 1 1]. However, in hydrothermally synthesized samples, the morphology is typically associated with the [1 0 0] and [1 1 1] facets. As shown in Figure SM-4 and Fig. 3, the Cu-doped $BaZrO_3$ samples also present a pronounced [1 1 0] facet. The observed morphology underscores the roles of doping and synthesis conditions in determining the structural characteristics of $BaZrO_3$, underscoring the hydrothermal method's ability to achieve unique, controlled crystal geometries. The uncalcined samples showed lower definition and coalescence (see Figure SM-4 and Fig. 3), with a more dispersed, less compact appearance. This behavior indicates that the absence of post-synthesis thermal treatment hinders complete crystallization or particle agglomeration, resulting in a less defined, powder-like structure with a more dispersed nature. Such a material is less consolidated, which could negatively affect its mechanical and functional properties [34]. Furthermore, a higher prevalence of smaller (primary) particles was observed. These smaller particles may be remnants of the synthesis process or primary particles that later coalesce to form larger secondary particles during thermal treatment. This suggests the importance of calcination in achieving a well-defined, consolidated structure with improved properties. In contrast, the calcined samples (Fig. 3) exhibited greater particle compaction and coalescence (see Table SM–2). The calcination process promotes particle bonding and coalescence, resulting in a better-defined morphology. The particles displayed sharper edges and more uniform shapes compared to the uncalcined samples. This indicates that thermal treatment facilitates sintering, enhancing structural coalescence and overall morphological definition.

A common feature observed across all samples is the presence of secondary particles larger structures formed through the agglomeration of primary particles. This phenomenon is particularly evident in the images of uncalcined samples (see Fig. SM–4). The results suggest that particle growth follows a hierarchical pattern, where smaller primary particles combine to form larger structures. These findings underscore the importance of thermal treatment in enhancing the material's morphological properties, promoting more consolidated, uniform structures. Measured N_2 adsorption–desorption isotherms (Fig. SM–5) for calcined $BaZrO_3$ samples yielded BET surface area estimates reported in Table 2. The results show type IV isotherms and mesoporousity [45]. The $BaZnO_3$ samples have larger BET surface areas than the undoped material, and the available surface area decreases with increasing Cu concentration. This is also reflected in the decrease in pore size.

3.4. UV–visible spectroscopy (DRS) studies

The optical absorbance spectra of the obtained barium zirconates ($BaZrO_3$) were evaluated using UV–vis spectroscopy in the wavelength range of 190–1100 nm, as shown in Fig. 4 and Figure SM6 (calcined and uncalcined samples, respectively). A distinct absorbance peak at 229 nm, for both calcined and uncalcined, is likely associated with charge-transfer processes involving electronic transitions in $BaZrO_3$, particularly those related to oxygen vacancies [46]. In Fig. 4, corresponding to the calcined samples, a modification in the absorbance profile is observed upon Cu doping. The characteristic peak ($\lambda = 400$ nm) of pristine $BaZrO_3$ not only intensifies but also strongly broadens in proportion to the Cu concentration. For the highest doping level, sample C–$BaZrO_3$:Cu (5.0 %), the original $BaZrO_3$ absorption peak ($\lambda = 229$ nm) is almost hindered by the broader and stronger band centered at 400 nm. This spectrum resembles that reported in the literature for Cu-doped samples, with a prominent peak appearing around 340 nm [26,47]. This suggests that the broad band centered at 400 nm is a superposition of the Cu bands around 340 nm and the $BaZrO_3$ defect band centered at 400 nm, and its stronger absorption and broader bandwidth may be related to the increasing number of defects introduced by the substitution of Cu ions within the $BaZrO_3$ lattice.

3.5. Electrochemical characterization

Electrochemical characterization was performed using a standard three-electrode setup. A platinum mesh was employed as the counter electrode, a saturated calomel electrode (SCE) was used as the reference electrode, and working electrodes were fabricated by depositing $BaZrO_3$ and $BaZrO_3$:Cu calcined materials onto a conductive FTO glass substrate using a screen-printing method. Electrochemical cyclic voltammetry (CV) was used to estimate the valence and conduction band positions of the materials. The onset potential and peak maxima were calculated in both the oxidation and reduction regions (Fig. 5), under visible-light irradiation (L, using a 75 W xenon lamp as the light source) and in the absence of light irradiation (D). These values are associated with the charge redistribution in the valence and conduction bands.

The electrochemical tests were conducted in a 0.1 M NaOH electrolyte, in an alkaline aqueous medium (pH 13). The Mott-Schottky test was performed over a frequency range from 100 Hz to 1 MHz, during which typical p-type semiconductor behavior was observed (see Fig. 6). The tests were carried out both in the presence and in the absence of light, using a 75 W xenon lamp as the light source.

The band gap energy ($\boldsymbol{E_g}$) was indirectly determined using cyclic voltammetry (CV). The electrochemical estimation of $\boldsymbol{E_g}$ is based on band-edge measurements: the flat-band potential $\boldsymbol{E_{fb}}$ determined by Mott–Schottky analysis and the oxidation/reduction onsets from cyclic voltammetry. These data allow inferring the conduction and valence band edges (CB/VB), and their separation defines the Electrochemical $\boldsymbol{E_g}$ [48]. In CV, the $\boldsymbol{E_g}$ is defined as the difference between the oxidation and reduction potentials, multiplied by the elementary charge of the electron [49]. Fig. 7 shows the $\boldsymbol{E_g}$ values obtained from both Mott-Schottky (MS) analysis and the electrochemical $\boldsymbol{E_g}$ derived from CV (see Fig. 6). A clear influence of Cu doping on the $BaZrO_3$ $BaZrO_3$ samples can be observed, where the $\boldsymbol{E_g}$ decreases linearly with increasing Cu concentration. The highest $\boldsymbol{E_g}$ was found for the pristine $BaZrO_3$ sample, with a value of 4.8 eV, while the smaller $\boldsymbol{E_g}$ was recorded for the C–$BaZrO_3$:Cu (5.0 %) sample, with a value of 3.4 eV. For all samples, the valence band (VB) and conduction band (CB) are located within the potential window required for hydrogen evolution, confirming their suitability for photocatalytic water splitting.

Chronoamperometry was performed to measure photocurrent intensity over time by applying a constant potential to the working electrode. The electrodes used in this study were $BaZrO_3$ calcined at 1100 °C, both pristine and doped with Cu at 0.5, 1.0, 2.5, and 5.0 at%. Measurements were taken at 60 s intervals in the dark and under illumination, for a total duration of 5 min. The applied potential was 0.40 V. The diffusion behavior of electroactive species in solution was analyzed, revealing an increase in the photoresponse of the materials under illumination, particularly during ionic diffusion at the working electrode. As shown in Fig. 8, the photocurrent increased upon light exposure but gradually decreased over time, following a typical chronoamperometric pattern. When the light source was turned off, no significant photocurrent was detected. However, an instantaneous photocurrent density was generated under illumination, confirming the electrodes' photosensitivity. Furthermore, the photocurrent density was found to depend on the Cu doping level. Among the tested samples, the $BaZrO_3$:Cu material doped at 0.5 % exhibited the highest photocurrent density.

The electron lifetime (τ) (see Table 3) was determined from the temporal variation of the intensity measured under open-circuit conditions, when the light source was turned off. In this case, the intensity increased when the light was switched off, indicating the release of trapped carriers. The relationship used was $\tau = \frac{nk_B T}{q}\left(\frac{1}{\frac{dV_{OC}}{dt}}\right)$, where k_B is the Boltzmann constant, T the absolute temperature, q the elementary charge of the electron and n the ideality factor, for the Cu-modified $BaZrO_3$ semiconductor, where recombination transitions are mainly

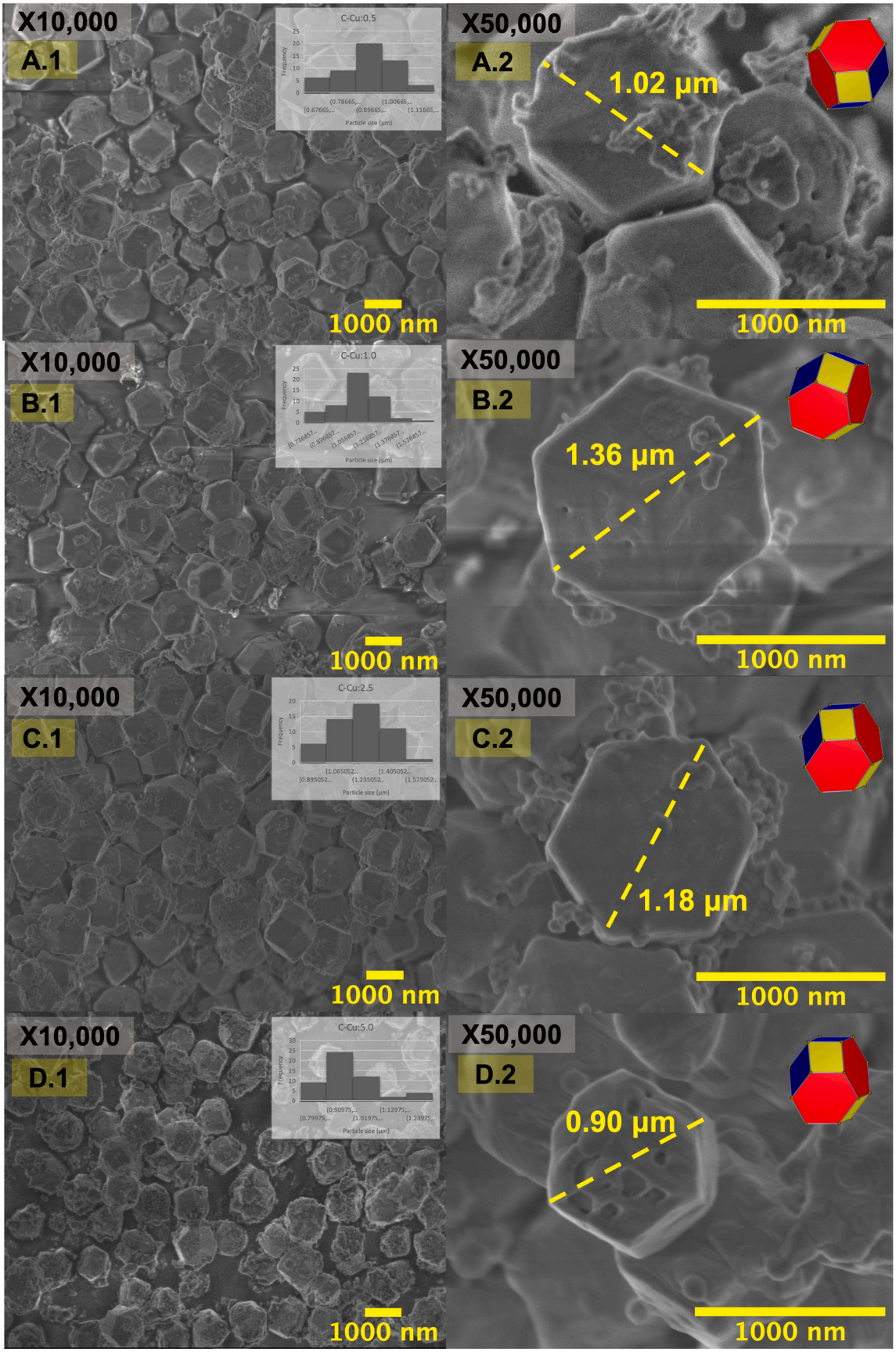

Fig. 3. SEM images of calcined $BaZrO_3$ nanoparticles obtained through the hydrothermal process, doped with Cu. A.1) Image at 10,000X of C–$BaZrO_3$:Cu(0.5 %). A.2) Image at 50,000X of C–$BaZrO_3$:Cu(0.5 %). B.1) Image at 10,000X of C–BaZrO3:Cu(1.0 %). B.2) Image at 50,000X of C–$BaZrO_3$:Cu(1.0 %). C.1) Image at 10,000X of C–$BaZrO_3$:Cu(2.5 %). C.2) Image at 50,000X of C–$BaZrO_3$:Cu(2.5 %). D.1) Image at 10,000X of C–$BaZrO_3$:Cu(5.0 %). D.2) Image at 50,000X of C–$BaZrO_3$:Cu (5.0 %).

Table 2
S_{BET}, Pore Volume and, Pore size obtained from N_2 adsorption–desorption isotherms (Fig. SM–5) of pristine and Cu-doped (0.5 %, 1.0 %, 2.5 %, 5.0 at%) calcined $BaZrO_3$.

Sample	S_{BET} (m^2/g)	Pore Volume (cc/g)	Pore size (Å)
C–$BaZrO_3$	19.04	$3.95X10^{-2}$	41.53
C–$BaZrO_3$:Cu(0.5 %)	19.35	$3.56X10^{-2}$	36.83
C–$BaZrO_3$:Cu(1.0 %)	16.23	$2.94X10^{-2}$	36.19
C–$BaZrO_3$:Cu(2.5 %)	15.27	$2.94X10^{-2}$	38.43
C–$BaZrO_3$:Cu(5.0 %)	13.15	$2.55X10^{-2}$	38.86

indirect, $n = 2$ is adopted as a valid approximation [50].

The electron lifetime is significantly longer in C–$BaZrO_3$:Cu(0.5 %). These results are consistent with those obtained from chronoamperometry measurements. The following equations can explain the importance of the electron lifetime in the photocatalytic water splitting process:

$$Photocatalyst + light \rightarrow h^+_{VB} + e^-_{CB} \quad \text{(Eq. 1)}$$

$$2H_2O + 4\,h^+_{VB} \rightarrow O_2 + 4H^+ \quad \text{(Eq. 2)}$$

$$2H^+ + 2e^-_{CB} \rightarrow H_2 \quad \text{(Eq. 3)}$$

When a photocatalyst absorbs light with an energy greater than or equal to in an aqueous solution, oxidation-reduction reactions occur (Eqs. (1)–(3)). The overall reaction produces O_2 and H_2. The longer the lifetime of the photogenerated electrons, the greater the probability that they will reach the surface and react to form H_2. In the case of C–$BaZrO_3$:Cu(0.5 %), the lifetime of the negative carriers in the conduction band was calculated to be approximately 19.9 ns (see Table 3), a value consistent with that reported in the literature [26,51]. The longer lifetime of the photogenerated electrons for sample C–$BaZrO_3$:Cu(0.5 %) suggests this sample has a higher potential for H_2 evolution in water splitting processes.

The Nyquist plot (Fig. 9) of the pure $BaZrO_3$ and Cu-doped $BaZrO_3$ samples (0.5, 1.0, 2.5, and 5.0 at.%), all calcined at 1100 °C, shows clear variations in impedance due to the combined effects of Cu incorporation and thermal treatment. The undoped $BaZrO_3$ exhibits a moderately sized semicircle, attributed to grain and grain-boundary resistance resulting from sintering at 1100 °C [49]. Upon incorporating 0.5 % Cu, the total impedance decreases notably, indicating enhanced charge transfer due to the generation of oxygen vacancies and improved ionic mobility. However, at 1.0 % Cu, the semicircle diameter increases, suggesting increased impedance due to the formation of trapping defects and potential barriers at grain boundaries. The highest impedance is observed for 2.5 % Cu, which could be due either to structural distortion and disorder of the perovskite lattice as a consequence of the incorporation of Cu into the $BaZrO_3$ lattice. The increased Cu content in the 5.0 % Cu sample shows a slight reduction in impedance but remains more resistive than the low-doped compositions. These results indicate an optimal doping level around 0.5 % Cu, where electrical conductivity improves without inducing excessive structural defects, in agreement with the increased electron lifetime observed for this sample. Similar trends have been reported in other perovskite-type oxides, where excessive dopant concentrations increase grain boundary resistance [26]. Overall, the data confirm that the electrical response of $BaZrO_3$ is critically governed by the balance between Cu content and the degree of densification achieved during calcination at 1100 °C.

3.6. XPS and ICP analysis

XPS (Fig. 10) and ICP analysis (Table 4) were used to determine the elemental composition of selected $BaZrO_3$ and Cu-doped $BaZrO_3$ samples. The survey spectrum confirms the presence of Ba, Zr, and O as the principal lattice constituents, along with Cu signals in the doped samples, demonstrating successful cation incorporation. In the Ba 3d region, the characteristic Ba^{2+} doublet appears at approximately 779–780 eV ($3d_5/_2$) and 794–795 eV ($3d_3/_2$), consistent with Ba–O bonding in $BaZrO_3$perovskites and indicating that the Ba oxidation state remains unchanged upon Cu doping [52].

The Zr 3d doublet, located near 181–182 eV and 183–185 eV (Fig. 10), corresponds to Zr^{3+}/Zr^{4+}species in the ZrO_6 octahedra, confirming that the local coordination environment of zirconium is preserved [52]. The O 1s signal centered at ~529–530 eV is attributed to lattice O^{2-} (Fig. 10), while the minor shoulder at higher binding energy (~531–532 eV) arises from surface hydroxyl or chemisorbed oxygen species, a feature typical of alkaline-earth perovskites [52]. The C 1s component at ~286.4 eV indicates the presence of carbon bonded to other elements, such as oxygen (C–O), which could originate from environmental adsorption of CO_2 during sample handling [51]. In the Cu 2p spectrum, the peak at 932.6–934.5 eV [53], accompanied by distinct shake-up satellites at 940–945 eV, is diagnostic of Cu^{2+} and Cu^{+} species rather than Cu^0, confirming that copper exists as Cu^{2+}/Cu^{+} substituting at the B-site within the perovskite lattice [54]. Collectively, these results demonstrate that Cu incorporation does not disrupt the $BaZrO_3$ perovskite framework while introducing localized electronic states that may enhance photocatalytic performance by facilitating charge-carrier

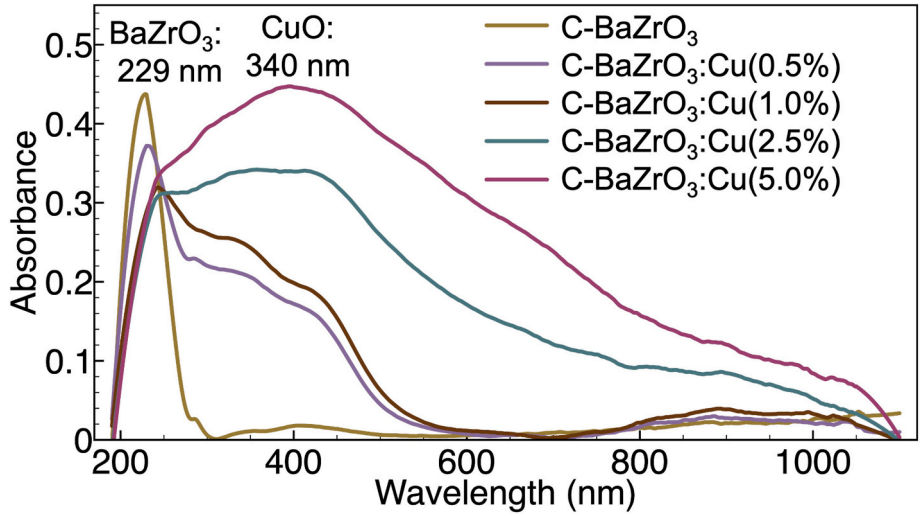

Fig. 4. UV–visible absorbance spectra of the calcined $BaZrO_3$ pristine and Cu-doped (0.5, 1.0, 2.5, and 5.0 at%) $BaZrO_3$ samples.

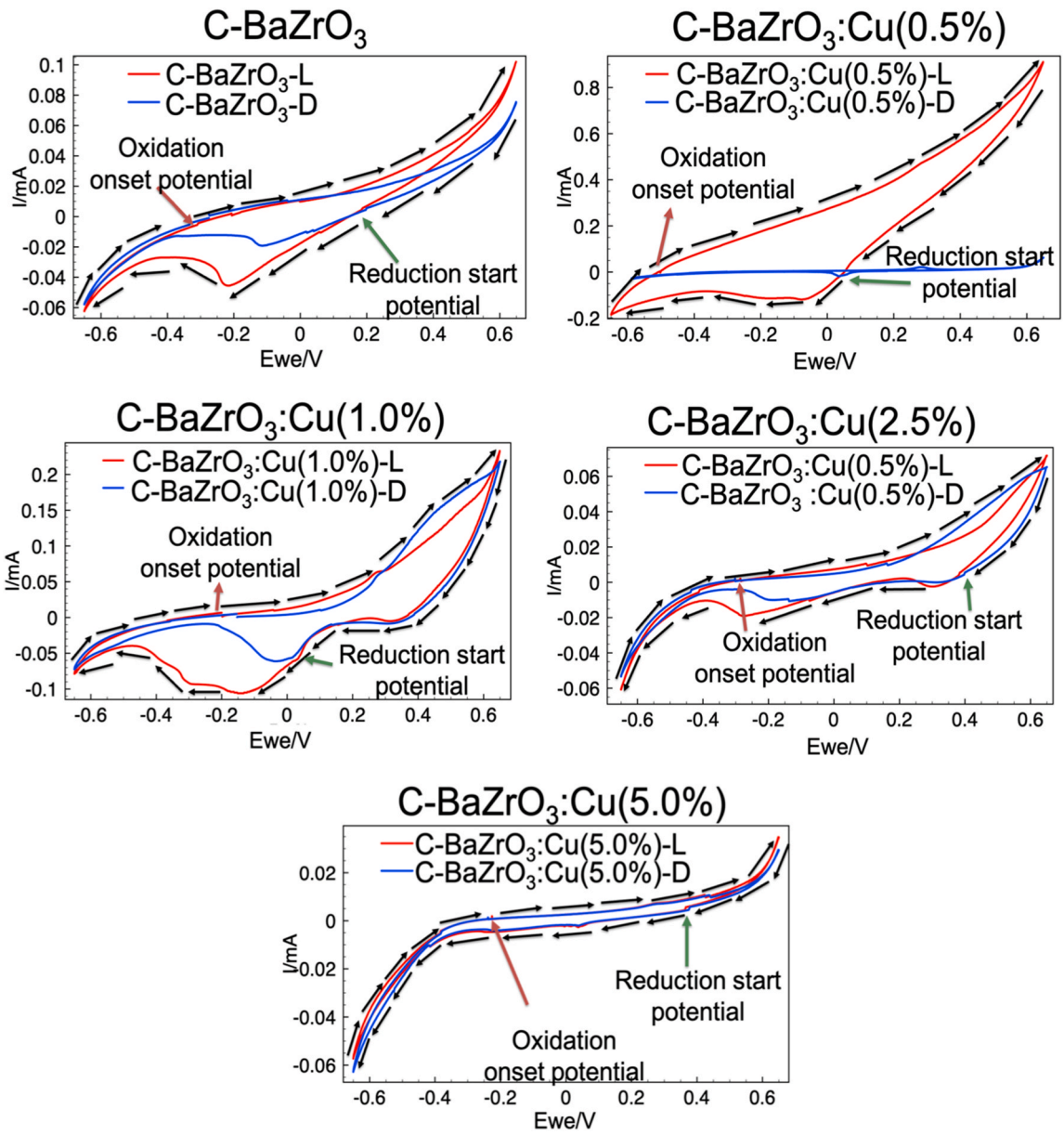

Fig. 5. CV to obtain the electrochemical E_g of $BaZrO_3$ pristine and Cu-doped (0.5, 1.0, 2.5, and 5.0 at%) $BaZrO_3$ samples in the presence of 75 W xenon-light (L) and absence of 75 W xenon-light (D).

separation, in agreement with the effects of Cu on the photogenerated electron lifetimes (see Table 3).

Additionally, Table 4 presents the ICP-OES results for the $BaZrO_3$ and Cu-doped $BaZrO_3$ samples. The experimental %at. Cu values are reasonably close to those estimated from theoretical stoichiometry. Minor deviations between theoretical and measured compositions are expected and can arise from factors such as sample preparation steps, calibration drift, matrix effects, and general uncertainties associated with ICP-OES quantification. These sources of variability have been well documented in the analytical chemistry literature, where both instrumental and operational factors contribute to measurement uncertainty in the determination of metallic elements [55]. To verify the reliability of the analytical procedure, the pristine $BaZrO_3$ sample was also included as a control. To determine the reliability of the ICP-OES analysis, the pristine $BaZrO_3$ sample was included. The reliability of the ICP-OES analysis is supported by the absence of a detectable signal for the Cu 2p orbitals in a pristine, undoped $BaZrO_3$ sample (see Fig. 10 and Table 4).

3.7. Photocatalytic hydrogen evolution

The hydrogen evolution yield from $BaZrO_3$ materials (Fig. 11), pristine and doped with Cu (0.5, 1.0, 2.5, and 5.0 at%), was evaluated in a Bach system in triplicate. The sample C–BaZrO3:Cu(0.5 %) exhibited the highest hydrogen evolution efficiency at 27.2 μmol g^{-1} h^{-1}, decreasing as Cu content increases. This behavior can be explained by the fact that high concentrations of Cu can disturb the crystal lattice, creating structural defects that negatively impact charge mobility, the conductivity, and stability [56]. Chronoamperometry (Fig. 8) confirmed that C–$BaZrO_3$:Cu(0.5 %) material exhibited the highest photocatalytic activity among all tested samples, along with a slight reduction in its $\boldsymbol{E_g}$. As observed in the Open Circuit Voltage (OCP) electrochemical tests (see Fig. SM–7), the electron lifetime is shorter as the Cu content increases (Table 3). Additionally, the electron lifetime is not the only important factor that could favor photocatalytic performance. As can be seen (Table 2), the BET area determined for the calcined materials is also consistent. The C–$BaZrO_3$:Cu(0.5 %) reached 19.35 m^3/g decreasing to

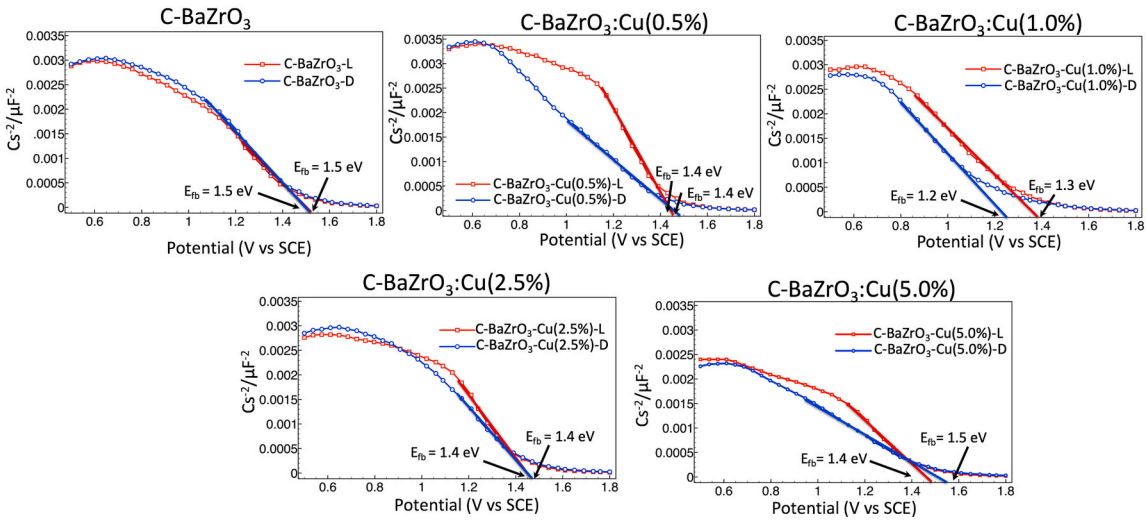

Fig. 6. Mott-Schottky plot of samples calcined at 1100 °C of pristine $BaZrO_3$ and (0.5, 1.0, 2.5, and 5.0 at%) Cu-doped $BaZrO_3$ samples in the presence of 75 W xenon-light.

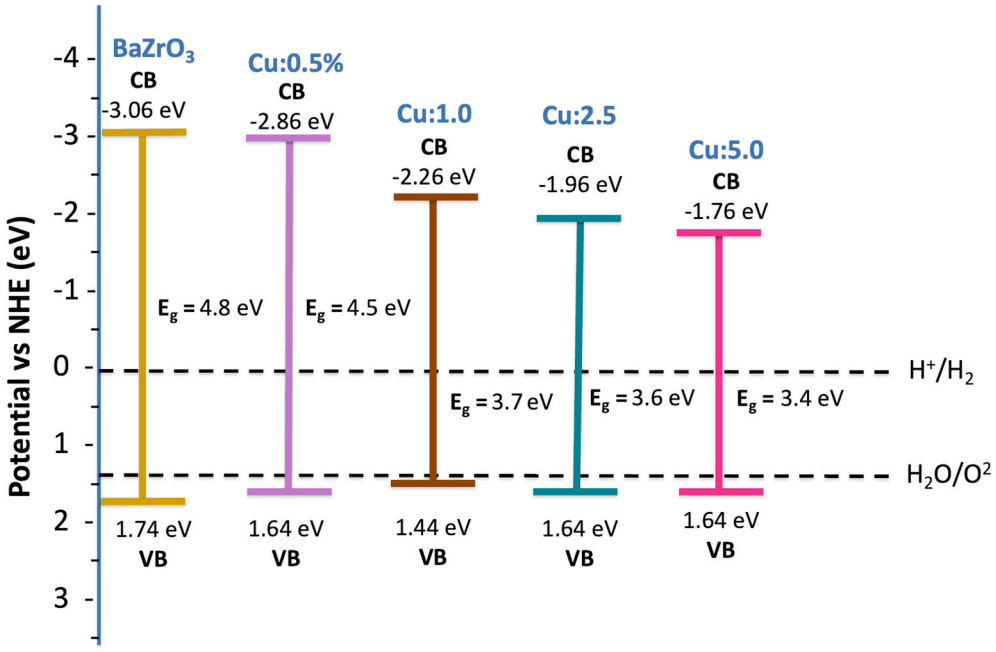

Fig. 7. Position plot of the valence and conduction bands of pristine ***BaZrO₃*** and Cu-doped C– ***BaZrO₃*** (0.5 %, 1.0 %, 2.5 %, and 5.0 at%). Calculated from Mott-Schottky and electrochemical E_g.

13.5 m^3/g in the mostly doped material (C–$BaZrO_3$:Cu(5.0 %)), however the bare material reached 41.64 m^3/g. Cu doping could slightly reduce the BET area relative to the undoped material, likely because Cu partly blocks pores or aggregates, reducing accessible surface [57].

The apparent quantum yield (AQY) was calculated according to the following equation [58].

$$AQY(\%) = \frac{2 \times N_{H_2}}{N_{incident\ photons}} \times 100 \qquad \text{(Eq. 4)}$$

Where N_{H_2} is the number of moles of evolved H_2, and the factor 2 accounts for the two electrons required per hydrogen molecule. The number of incident photons was calculated from the UV lamp irradiance ($\lambda = 254$ nm), the illuminated reactor area, and the exposure time. This approach follows standard procedures for evaluating intrinsic photocatalytic efficiency under sacrificial-free conditions, ensuring that the measured hydrogen evolution arises solely from the material's charge-separation and transfer capabilities [59,60].

From Table 5, it is observed that pristine $BaZrO_3$ and Cu-doped $BaZrO_3$ (0.5–5.0 at.%) exhibit apparent quantum yields (AQY) in the ≈0.32–0.54 % range, with a maximum near 0.54 % for 0.5 at%. Cu doped material and a slight decline at higher Cu contents. This trend indicates an optimal doping window in which moderate introduction of acceptor states/oxygen vacancies promotes charge separation. In contrast, excess Cu can generate recombination centers (e.g., segregated CuO) that penalize performance. Under 254 nm irradiation for 120 min, these efficiencies are on the same order of magnitude as those reported for other hydrothermally synthesized perovskites operated under visible light. However, they remain below those achieved by optimized $BaZrO_3$ systems in the literature [61].

In the literature, perovskite-based materials exhibit comparable

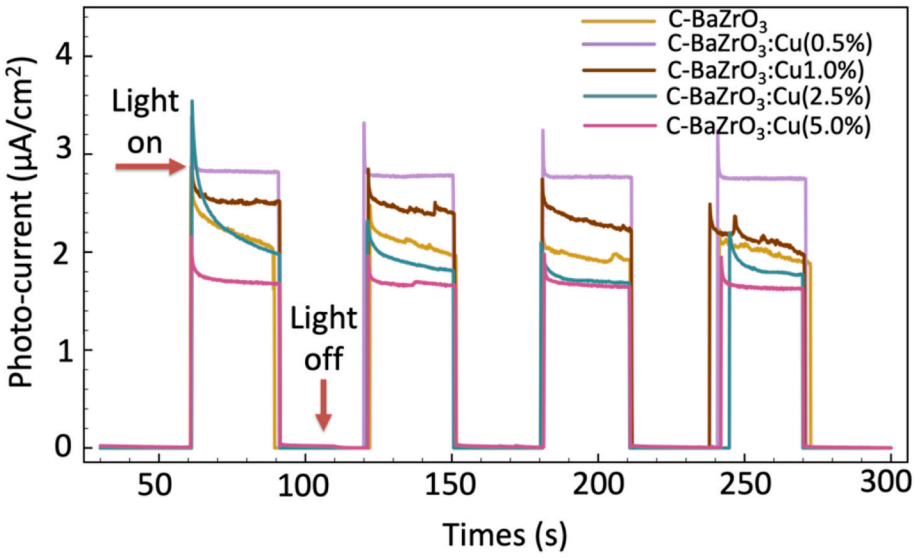

Fig. 8. Chronoamperometry measurements with light on/off of samples calcined at 1100 °C of $BaZrO_3$ and $BaZrO_3$ doped with Cu (0.5 %, 1.0 %, 2.5 %, and 5.0 %at).

Table 3
Electron lifetime of the samples calcined at 1100 °C of $BaZrO_3$ and $BaZrO_3$ doped with Cu (0.5 %, 1.0 %, 2.5 %, and 5.0 %at).

Sample	$\frac{dV_{OC}}{dt}$	τ (ns)
C–$BaZrO_3$	0.0268	1.92
C–$BaZrO_3$:Cu(0.5 %)	0.0026	19.89
C–$BaZrO_3$:Cu(1.0 %)	0.0028	18.47
C–$BaZrO_3$:Cu(2.5 %)	0.0090	5.74
C–$BaZrO_3$:Cu(5.0 %)	0.0045	11.49

hydrogen production rates. For example, $MgTiO_3$, a widely studied oxide perovskite, has demonstrated hydrogen production rates of up to 13.6 mmol g^{-1} h^{-1} [62]. Similarly, a MoS_2/$CsBiI_3$-based photocatalyst achieved a hydrogen evolution rate of 6.09 mmol g^{-1} h^{-1} in a mixed solution of ethanol and H_2O/H_3PO_4 [63]. Additionally, MoS_2-based perovskites have been reported to achieve hydrogen evolution rates of 13.6 mmol g^{-1} h^{-1} under visible-light irradiation [64]. In contrast, our experiments were conducted without any sacrificial agent or noble-metal co-catalyst in the photocatalytic reaction, and under UV irradiation from a low-power (400 μW) Hg pen lamp. Table 6 presents other works that do not use a sacrificial agent. As shown, the efficiency achieved in this work is competitive with those reported in similar photocatalytic studies using more complex materials. In this work, an AQY% = 0.54 for C–$BaZrO_3$:Cu(0.5 %) was achieved without the addition of sacrificial agents or co-catalysts. For example, Xiao and co-workers evaluated the performance of Zirconium-Doped TaON, a perovskite with similar characteristics, and obtained conversion efficiencies of 0.66 % Xiao et al. [65]. More complex materials, such as Zr-doped $BaTaO_2N$ + $BiVO_4$, have been reported to have an AQY of 0.4 % using methanol as the sacrificial agent [66].

In addition to its higher hydrogen evolution rate, barium zirconate ($BaZrO_3$) offers several key advantages over other perovskite-based photocatalysts, such as $MgTiO_3$ and MoS_2/$CsBiI_3$, making it an attractive material for practical, long-term hydrogen production. First, $BaZrO_3$ exhibits remarkable chemical and environmental stability [26]. Unlike hybrid halide perovskites (e.g., $CsPbI_3$ and $CsBiI_3$), which are prone to degradation under humidity and light exposure, $BaZrO_3$ maintains its structural and optical integrity in aqueous and photochemical environments. This stability significantly enhances the material's durability in photocatalytic systems. Second, $BaZrO_3$ is composed of non-toxic elements [73]. In contrast, perovskites such as $CsPbI_3$ and $CsBiI_3$ incorporate lead and bismuth, respectively, elements that pose environmental and health risks due to their bioaccumulative and toxic properties.

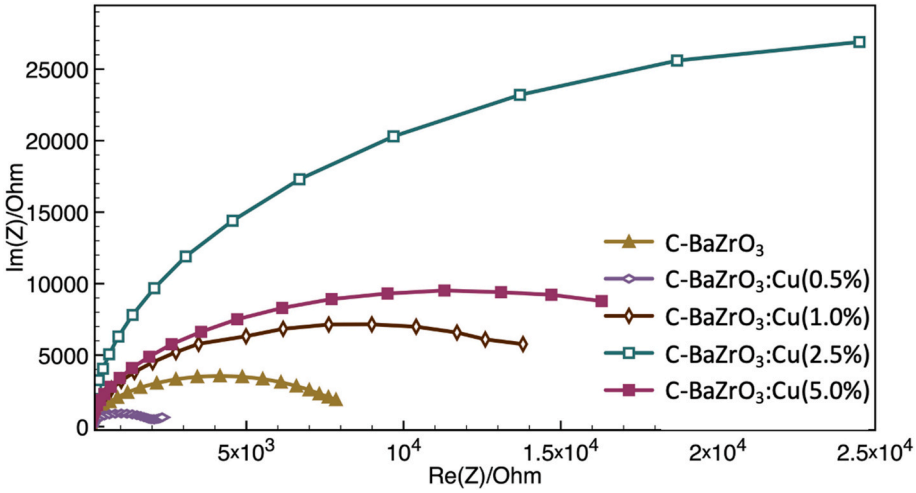

Fig. 9. Nyquist diagrams for the $BaZrO_3$ and Cu-doped $BaZrO_3$ sample (0.5 %, 1.0 %, 2.5 % and 5.0 at%).

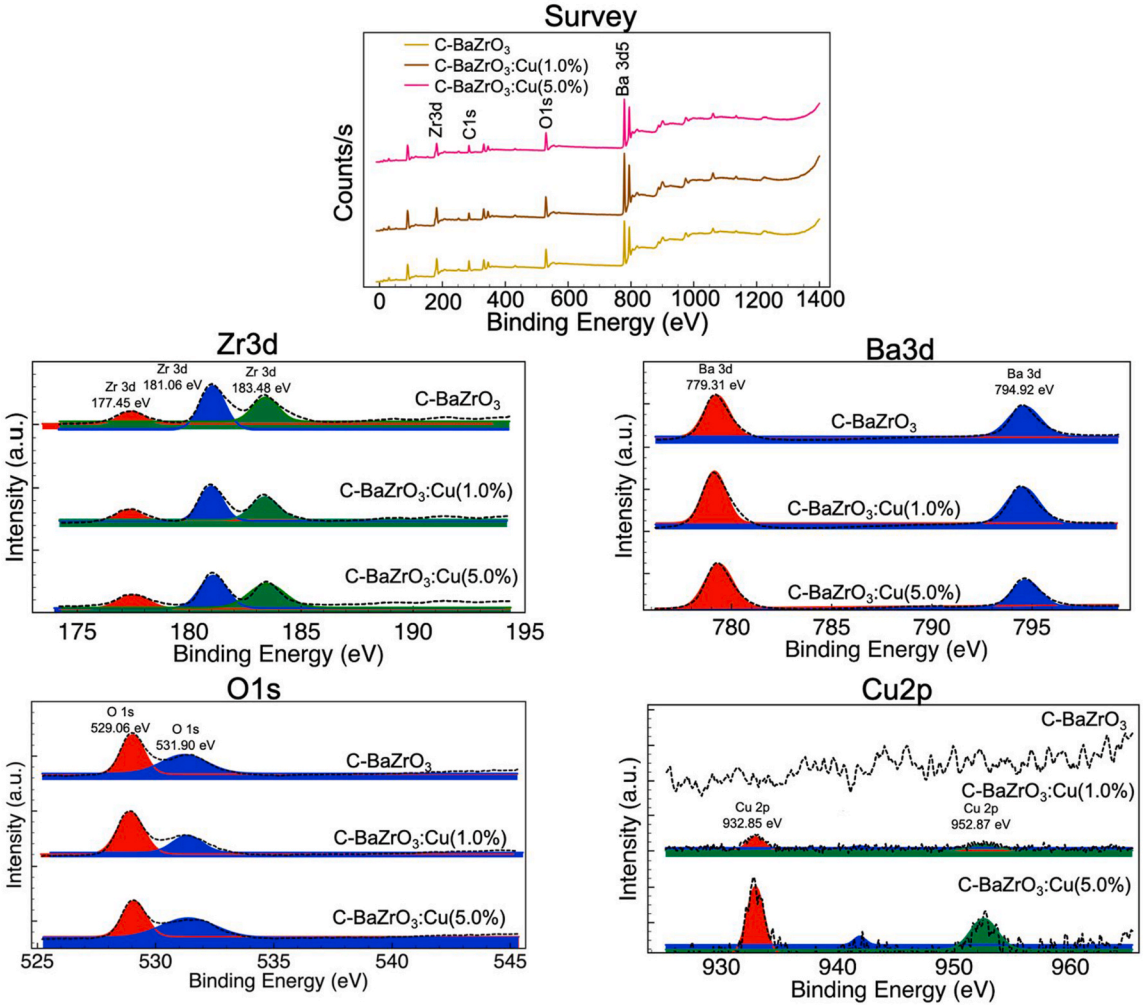

Fig. 10. XPS survey spectra and corresponding high-resolution XPS spectra for the $BaZrO_3$ and Cu-doped $BaZrO_3$ samples (1.0 % and 5.0 at%).

Table 4
Cu at% of $BaZrO_3$, C–$BaZrO_3$:Cu(1.0 %) and C–$BaZrO_3$:Cu(5.0 %) samples measured by ICP-OES analysis.

Sample	Concentration of Cu obtained by ICP-OES
$BaZrO_3$	Undetectable
C–$BaZrO_3$:Cu(1.0 %)	1.02 %
C–$BaZrO_3$:Cu(5.0 %)	4.91 %

Third, $BaZrO_3$ is cost-effective due to the abundance and relatively low cost of its constituent elements [74]. In comparison, materials such as MoS_2 and $CsBiI_3$ contain more expensive or less abundant elements, such as molybdenum, iodine, or bismuth, which can increase the overall synthesis and scaling costs of photocatalytic systems. Furthermore, $BaZrO_3$ features a robust perovskite crystal structure that withstands high temperatures and harsh chemical environments without significant degradation.

3.8. Hydrogen evolution mechanism for $BaZrO_3$:Cu

The mechanism of water splitting by $BaZrO_3$:Cu involves two half-reactions: the hydrogen evolution reaction (by the photogenerated e^-) and the oxygen evolution reaction (by the photogenerated h^+). Perovskite-based catalysts can drive both reactions, using light to generate charge carriers. The possible photocatalytic mechanism of water splitting by $BaZrO_3$:Cu is presented in Fig. 12. The kinetic mechanism for H_2 production can be summarized in three steps: i) absorption of light with an energy equal to or greater than the E_g of $BaZrO_3$:Cu and charge separation within the material, ii) charge transfer to the H_2O molecules, and iii) splitting of the H_2O molecule with the consequent generation of H_2 and O_2. As shown in Fig. 4, light absorption improves with the inclusion of Cu atoms, decreasing the E_g of the material and achieving an optimal concentration of 0.5 at%. The Cu atoms also increase the surface area, increasing the number of reaction sites and enhancing charge transfer to the solution. These are the three main changes that, together, improve the performance of $BaZrO_3$:Cu(0.5 %) materials. Recent studies show that an M-*O*-M angle near 180° enhances the delocalization of the activation energy [75]. As mentioned by Yupeng and collaborators [76]. $BaZrO_3$ has a 180° Zr–*O*–Zr angle; consequently, the photogenerated electrons move more readily, facilitating electron-hole transfer and thereby promoting photocatalytic activity. The good photocatalytic activity of $BaZrO_3$:Cu is also supported by XPS studies showing that Cu^{2+} replaces the B sites in the perovskite without deforming its structure, but introduces electronic states that favor charge separation, increase electron lifetime, and thereby improve the photocatalytic activity.

The possible kinetic reaction steps are described as follows:

$$BaZrO_3 : Cu \xrightarrow{h\nu} BaZrO_3 : Cu\left(e^-_{CB} + h^+_{VB}\right) \quad \text{(Eq 5)}$$

$$H_2O + V_o \rightarrow 2H^+ + O^{2-} \quad \text{(Eq 6)}$$

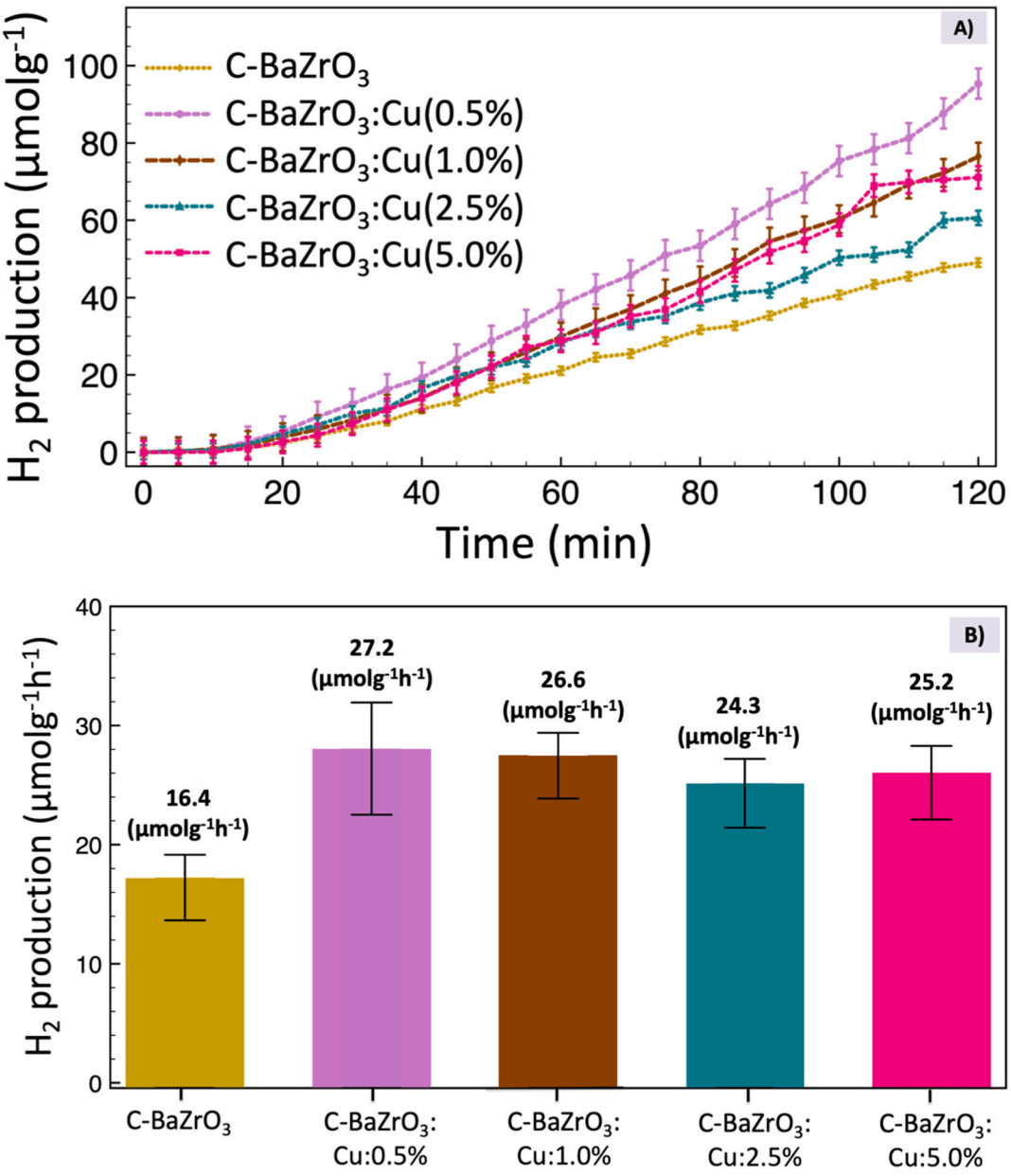

Fig. 11. A) Photocatalytic H_2 evolution profile from calcined pristine and Cu-doped $BaZrO_3$ (0.5, 1.0, 2.5, and 5.0 at%). B) Photocatalytic H_2 production rate from calcined pristine and Cu-doped $BaZrO_3$ (0.5, 1.0, 2.5, and 5.0 at%) during 2 h. Photocatalytic conditions: 50 mg of catalyst, 200 mL of deionized water, irradiation source: Hg pencil lamp at 254 nm. H_2 evolution test was conducted in triplicate.

Table 5
Hydrogen generation rates and efficiencies of pristine and Cu-doped (0.5 %, 1.0 %, 2.5 %, 5.0 at%) calcined $BaZrO_3$.

Sample	H_2 rate (µmol g^{-1} h^{-1})	Total H_2 per test, β (µmol)	AQY (%)
C–$BaZrO_3$	16.4	1.64	0.32
C–$BaZrO_3$:Cu(0.5 %)	27.2	2.72	0.54
C–$BaZrO_3$:Cu(1.0 %)	26.6	2.66	0.52
C–$BaZrO_3$:Cu(2.5 %)	24.3	2.43	0.48
C–$BaZrO_3$:Cu(5.0 %)	25.2	2.52	0.50

$$2H^+ + e^-_{CB} \rightarrow H_2\uparrow \quad \text{(Eq 7)}$$

$$H_2O + V_o + 2e^-_{CB} \rightarrow H_2\uparrow + O^{2-} \quad \text{(Eq 8)}$$

Upon UV–Vis irradiation, $BaZrO_3$:Cu becomes photoexcited, leading to the generation of electron–hole pairs (Eq. (4)). The presence of oxygen vacancies (V_o) provides active adsorption sites for H_2O molecules, inducing a distortion in their molecular symmetry. This interaction facilitates the formation of reactive oxygen species (Eq. (5)) by oxygen trapping and weakening the O–H bond. The subsequent bond cleavage produces H^+ ions, which are reduced by photoexcited electrons to yield molecular hydrogen (H_2). Therefore, materials possessing a higher density of oxygen vacancies and improved surface and optoelectronic properties are expected to enhance H^+ generation and, consequently, H_2 evolution during water photocatalysis. Furthermore, the electronic coupling between the Cu^{2+} states and the $BaZrO_3$ conduction band serves as a charge-transfer mediator, promoting the overall water-reduction process.

Table 6
State-of-the-art comparison of photocatalytic hydrogen generation.

Material (best sample)	Type of material	Sacrificial agent(s)	Light source/key conditions	Catalyst mass	Reactor volume/ solution	Time	H_2 detection method	H_2 activity (as reported)	AQE/AQY (%)	Ref.
$BaTaO_2N$ (RbCl route) + Rh/ Cr_2O_3/IrO_2	Perovskite oxynitride	Pure water	300 W Xe lamp ($\lambda >$ 420 nm)	Not reported	150 ml Pure water	0.5–20 h	gas chromatograph (GC 8 A, Shimadzu, with a thermal conductivity detector, molecular sieve 5 A column and Ar as the carrier gas).	1.6 μmol h^{-1}	AQY ~0.1 % @ 400 nm	[67]
Zr-doped TaON (Ru/Cr_2O_3/IrO_2 cocatalysts)	Oxynitride (TaON)	Pure water	Visible (420 nm)	150 mg	150 ml	3 h	Not reported	9 μmol	0.66 % @ 420 nm	[65]
3D porous g-C_3N_4 nanosheets	Polymeric carbon nitride (PCN)	Pure water	300 W Xe lamp with a cutoff filter ($\lambda \geq$ 420 nm)	50 mg	100 ml	Up to ~100 h (stability)	Gas chromatography equipped with a thermal conductive detector (TCD)	49.1 μmol g −1 h −1	1.4 % @ 420 nm	[68]
$LaMg_xTa_{1-x}O_1+3_xN_2-3_x$	perovskite oxynitride	40 mL of distilled water + Ti peroxide solution (≈200 μL)	300 W Xe lamp (300 nm)	80 mg	40 ml	10 h	Gas chromatography (Shimadzu GC-8A)	0.032 fFμmol	0.03 % @ 420 nm	[69]
Fluorinated g-C_3N_4 (F-0.1-CN)	Polymeric carbon nitride (single-phase)	None (pure water)	300 W Xe ($\lambda \geq$ 300 nm)	30 mg	100 mL pure water	5 h	GC-TCD with 5 Å molecular sieve; carrier Ar. (GC-MS Agilent 7890B–5977B only for isotope tests)	177.79 μmol g^{-1} h^{-1} (white light); 83.89 μmol g^{-1} h^{-1} (AM1.5G)	AQY = 0.0164 % @ 420 nm	[70]
$SrTiO_3$:Ir,Sb,Al + $RhCrO_x$ (visible OWS)	Perovskite oxide (multi-doped $SrTiO_3$)	None (pure water)	300 W Xe, $\lambda >$ 440 nm	0.20 g	120 mL pure water	5 h	Not reported	62 μmol h^{-1} H_2 (absolute production rate)	AQY = 0.73 % @ 420 nm	[61]
Zr-doped $BaTaO_2N$ + $BiVO_4$ (ZOWS)	Oxynitride + oxide (Z-scheme)	pure water + methanol (15 vol %)	300 W Xenon (420 nm)	100 mg	150 mL	10 h	Gas chromatography (GC; Shimadzu, GC-8A)	37 mmol h^{-1}	AQY = 0.4 % @ 420 nm	[66]
Mo-/O-deficient $Bi_2Mo_3(S,O)_{12}$ (BiMoOS-2)	Bimetallic oxysulfide with O vacancies	Na_2S (10 mmol) + Na_2SO_3 (10 mmol) in 50 mL	Xe 250 W, 420 nm filter, visible light	25 mg	50 mL	4 h	Gas chromatograph PANNA-A91, Ar 99.999 %	480.87 μmol h^{-1} (≈19.2 mmol g^{-1} h^{-1})	14.26 % (420 nm)	[58]
Mo(S,O)/Co(O,S) (MoCoOS-2)	Heterojunction oxysulfide (Z-scheme)	Na_2S (10 mmol) + Na_2SO_3 (10 mmol)	Xe 150 W, $\lambda <$ 420 nm	20 mg	400 mL reactor, 50 mL water	4 h per cycle (6 cycles)	GC (PANNA A91) Ar carrier	153.4 mmol h^{-1} (max.), STH ≈ 0.25 %	14.42 %	[71]
Au–P25–CRIS (Au NP size ≈ 5.7 nm)	TiO_2 (P25) decorated with finely size-tailored Au nanoparticles	Oxalic acid (50 mM)	UV fluorescent lamps, 10 × 15 W, λ = 365 nm, N_2-purged aqueous suspension	150 mg	150 mL water + 50 mM oxalic acid	2 h (sampling every 10–20 min)	Gas chromatography (HP 5890 GC, TCD, MS-5Å column, N_2 carrier gas)	1.546 × 10^{-6} mol L^{-1} s^{-1}	4.86 % AQY at 365 nm	[72]
BaZrO3:Cu(0.5 %)	Perovskite oxide	Pure water	UV pen lamp (254 nm)	50 mg	200 mL	2 h	Gas chromatograph (Shimadzu GC-2014)	27.2 μmol g^{-1} h^{-1}	0.54 % @ 254 nm	This work

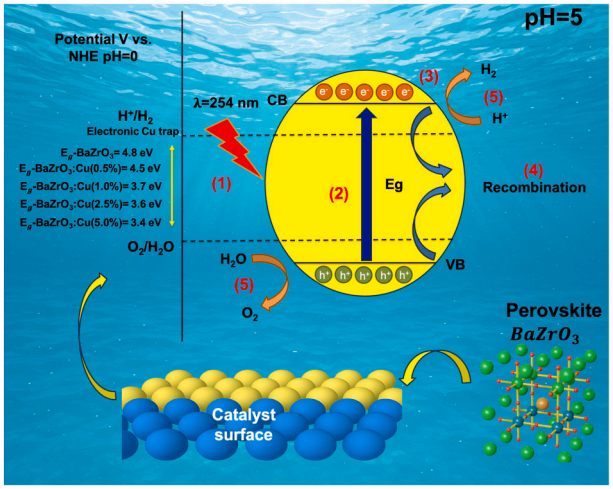

Fig. 12. Proposal mechanism of hydrogen evolution by photocatalysis with $BaZrO_3$:Cu structures.

4. Conclusions

$BaZrO_3$ was synthesized by the sol-gel method with varying amounts of Cu to drive photocatalytic water splitting in a batch system under light from 400 μW Hg pen lamp. This study shows the potential of Cu-doped $BaZrO_3$ as an efficient photocatalyst for hydrogen evolution via photocatalytic water splitting. Characterization confirmed that Cu incorporation effectively narrowed the E_g and enhanced charge carrier separation, thereby improving photocatalytic performance. Although calcination improved crystallinity and phase purity, it did not lead to a substantial increase in photocatalytic hydrogen production. The calcined sample C–$BaZrO_3$:Cu:0.5 % exhibited the highest hydrogen evolution rate, reaching 27.2 μmol g^{-1} h^{-1}, while its uncalcined counterpart. At higher Cu concentrations (>1.0 %), uncalcined samples formed secondary phases, impairing charge separation. This highlights the importance of optimizing dopant content, as excess Cu can lead to structural defects and increased electron-hole recombination. Cu doping is a highly effective strategy for tuning the electronic structure and enhancing the photocatalytic performance of $BaZrO_3$, particularly at low doping levels.

CRediT authorship contribution statement

Catalina Vega-Reyes: Writing – review & editing, Writing – original draft, Methodology, Investigation, Formal analysis. **Iliana E. Medina-Ramírez:** Writing – review & editing, Visualization, Supervision. **Luis A. Díaz-Torres:** Writing – review & editing, Supervision, Resources, Methodology. **Eduardo Coutiño-González:** Writing – review & editing, Supervision. **Patricia M. Olmos-Moya:** Writing – review & editing, Visualization, Resources. **Carlos A. Pineda-Arellano:** Writing – review & editing, Writing – original draft, Project administration, Funding acquisition, Conceptualization.

Conflict of interest

The authors declare that they have no known competing financial interest or personal relationships that could have to influence the work reported in this paper.

Acknowledgements

This work was partially funded by Secihti Project CBF2023-2997. M. Christian Albor Cortes made the technical characterization of SEM and XRD. M. Catalina Vega Reyes is grateful to Secihti for the grant (CVU: 932092) to carry out PhD studies at CIO-Unidad Aguascalientes.

Appendix A. Supplementary data

Supplementary data to this article can be found online at https://doi.org/10.1016/j.jics.2025.102386.

References

[1] X. Li, et al., Catalytic cracking of biomass tar for hydrogen-rich gas production: parameter optimization using response surface methodology combined with deterministic finite automaton, Renew. Energy 241 (Mar. 2025) 122368, https://doi.org/10.1016/j.renene.2025.122368.
[2] Bing Zhang, Sui-Xin Zhang, Rui Yao, Yong-Hong Wu, Jie-Shan Qiu, Progress and prospects of hydrogen production: opportunities and challenges, J. Electron. Sci. Technol. 19 (2) (June 2021) 100080, https://doi.org/10.1016/j.jnlest.2021.100080.
[3] M. Asad, et al., Facile synthesis of MnS/NiO heterostructure to enhance the water electrocatalysis for clean energy production, J. Indian Chem. Soc. 102 (5) (May 2025) 101646, https://doi.org/10.1016/j.jics.2025.101646.
[4] A. Ajanovic, M. Sayer, R. Haas, The economics and the environmental benignity of different colors of hydrogen, Int. J. Hydrogen Energy 47 (57) (July 2022) 24136–24154, https://doi.org/10.1016/j.ijhydene.2022.02.094.
[5] A. Fluri, et al., Enhanced proton conductivity in Y-Doped BaZrO3 via strain engineering, Adv. Sci. 4 (12) (2017) 1700467, https://doi.org/10.1002/advs.201700467.
[6] Wenhuan Huang, et al., Isolated electron trap-induced charge accumulation for efficient photocatalytic hydrogen production, Ger. Chem. Socieyt (Apr. 2023), https://doi.org/10.1002/anie.202304634.
[7] F. Xu, B. Weng, Photocatalytic hydrogen production: an overview of new advances in structural tuning strategies, J. Mater. Chem. A 11 (9) (Feb. 2023) 4473–4486, https://doi.org/10.1039/D2TA09614E.
[8] Muhammad Tayyab, et al., A new breakthrough in photocatalytic hydrogen evolution by amorphous and chalcogenide enriched cocatalysts, Chem. Eng. J. 455 (140601) (Jan. 2023) 1–20, https://doi.org/10.1016/j.cej.2022.140601.
[9] Xinlong Zheng, et al., ZnIn2S4-based photocatalysts for photocatalytic hydrogen evolution via water splitting, Coord. Chem. Rev. 475 (214898) (Jan. 2023) 1–27, https://doi.org/10.1016/j.ccr.2022.214898.
[10] Aayush Gupta, Blaž Likozar, Runia Jana, Wairakpam Chinglembi Chanu, Mahesh Kumar Singh, A review of hydrogen production processes by photocatalytic water splitting – from atomistic catalysis design to optimal reactor engineering, Int. J. Hydrogen Energy 47 (78) (Sept. 2022) 33282–33307, https://doi.org/10.1016/j.ijhydene.2022.07.210.
[11] Nan Xiao, Songsong Li, Xuli Li, Lei Ge, Yangqin Gao, Ning Li, The roles and mechanism of cocatalysts in photocatalytic water splitting to produce hydrogen, Chin. J. Catal. 41 (4) (Apr. 2020) 642–671, https://doi.org/10.1016/S1872-2067(19)63469-8.
[12] B. Abhishek, et al., Challenges in photocatalytic hydrogen evolution: importance of photocatalysts and photocatalytic reactors, Int. J. Hydrogen Energy 81 (4) (Sept. 2024) 1442–1466, https://doi.org/10.1016/j.ijhydene.2024.07.262.
[13] Jakob Schlenkrich, et al., Investigation of the photocatalytic hydrogen production of semiconductor nanocrystal-based hydrogels, Small 19 (2208108) (Feb. 2023) 1–12, https://doi.org/10.1002/smll.202208108, 21.
[14] M.F. Abou Taleb, H.A. Albalwi, M.M. Ibrahim, A synergistic advancement of rGO-supported perovskite oxide composite for sustainable energy system, J. Indian Chem. Soc. 102 (7) (July 2025) 101757, https://doi.org/10.1016/j.jics.2025.101757.
[15] S. Karadirek, B. Turan, P. Demircivi, Construction of BaZrO3/chitosan composite for sufficient antibiotic adsorptive removal: central composite design analysis and antimicrobial performance, J. Indian Chem. Soc. 102 (8) (Aug. 2025) 101813, https://doi.org/10.1016/j.jics.2025.101813.
[16] Hui-Zhen Shen, Ning Guo, Ping Shen, Synthesis and densification of BaZrO3 ceramics by reactive cold sintering of Ba(OH)2·8H2O-Zr(OH)4 powders author links open overlay panel, J. Eur. Ceram. Soc. 43 (2) (Feb. 2023) 392–400, https://doi.org/10.1016/j.jeurceramsoc.2022.10.016.
[17] R.I. López-Esquivel, et al., Green synthesis, structural and luminescent characterization of BaZrO3:Eu3+ nanoparticles, Ceram. Int. 49 (1) (Jan. 2023) 413–418, https://doi.org/10.1016/j.ceramint.2022.09.004.
[18] Q. Jiang, Y. Ma, P. Zhao, X. Li, Y. Shao, X. Xu, Electronic structure regulation of Fe sites by coordinating moieties in the fenton-like process enables tunable water decontamination, Environ. Sci. Technol. 59 (27) (July 2025) 14182–14192, https://doi.org/10.1021/acs.est.5c06061.
[19] R. Borja-Urby, L.A. Díaz-Torres, P. Salas, E. Moctezuma, M. Vega, C. Ángeles-Chávez, Structural study, photoluminescence, and photocatalytic activity of semiconducting BaZrO3:Bi nanocrystals, Mater. Sci. Eng. B 176 (17) (Oct. 2011) 1382–1387. https://doi.org/10.1016/j.mseb.2011.01.024.
[20] Z. Li, et al., Determination of Mn valence states in nanocatalysts during sustainable syngas conversion, J. Am. Chem. Soc. 147 (36) (Sept. 2025) 32548–32559, https://doi.org/10.1021/jacs.5c06550.
[21] S. Akhtar, et al., Investigation of structural, electronic and optical properties of (V+P)-Doped BaZrO3 for photocatalytic applications using density functional theory, J. Phys. Chem. Solid. 147 (Dec. 2020) 109662, https://doi.org/10.1016/j.jpcs.2020.109662.

[22] F.M. Draber, J.R. Denninger, P.C. Müller, I.K. Sommerfeld, M. Martin, The impact of nanoscale percolation in yttrium-doped BaZrO3 on the oxygen ion and proton conductivities: a density functional theory and kinetic monte carlo study, Adv. Energy Sustain. Res. 3 (8) (2022) 2200007, https://doi.org/10.1002/aesr.202200007.
[23] M. François, F. Demoisson, M. Sennour, G. Caboche, Continuous hydrothermal synthesis in supercritical conditions as a novel process for the elaboration of Y-doped BaZrO3, Ceram. Int. 47 (12) (June 2021) 17799–17803, https://doi.org/10.1016/j.ceramint.2021.03.044.
[24] H. Niu, et al., On the anomalous diffusion of proton in Y-doped BaZrO3 perovskite oxide, Solid State Ionics 376 (Mar. 2022) 115859, https://doi.org/10.1016/j.ssi.2022.115859.
[25] S.M. Alay-e-Abbas, F. Javed, G. Abbas, N. Amin, A. Laref, Density functional theory evaluation of ceramics suitable for hybrid advanced oxidation processes: a case study for Ce4+-Doped BaZrO3, J. Phys. Chem. C 123 (10) (Mar. 2019) 6044–6053, https://doi.org/10.1021/acs.jpcc.8b12221.
[26] Anindya Sundar Patra, Gaurangi Gogoi, Mohammad Qureshi, Ordered–disordered BaZrO 3−δ hollow nanosphere/carbon dot hybrid nanocomposite: a new visible-light-driven efficient composite photocatalyst for hydrogen production and dye degradation, ACS Omega 3 (9) (Sept. 2018) 10980–10991, https://doi.org/10.1021/acsomega.8b01577.
[27] A.S. Patra, et al., Combined experimental and theoretical insights into the synergistic effect of cerium doping and oxygen vacancies in BaZrO3−δ hollow nanospheres for efficient photocatalytic hydrogen production, J. Phys. Chem. C 123 (1) (Jan. 2019) 233–249, https://doi.org/10.1021/acs.jpcc.8b10626.
[28] H. Zhang, et al., Preparation of Ce4+-doped BaZrO3 by hydrothermal method and application in dual-frequent sonocatalytic degradation of norfloxacin in aqueous solution, Ultrason. Sonochem. 42 (Apr. 2018) 356–367, https://doi.org/10.1016/j.ultsonch.2017.11.043.
[29] S. Yilmaz, B. Kavici, P. Ramakrishnan, C. Celen, B.A. Horri, Highly conductive Cerium- and neodymium-doped barium zirconate perovskites for protonic ceramic fuel cells, Energies 16 (11) (2023) 1–14.
[30] K.P. Remya, D. Prabhu, R.J. Joseyphus, A.C. Bose, C. Viswanathan, N. Ponpandian, Tailoring the morphology and size of perovskite BiFeO3 nanostructures for enhanced magnetic and electrical properties, Mater. Des. 192 (July 2020) 108694, https://doi.org/10.1016/j.matdes.2020.108694.
[31] Pankaj P. Khirade, Shankar D. Birajdar, S.P. Jadhav, K.M. Jadhav, Sol-gel auto combustion synthesis of barium zirconate (BaZrO3) nanocrystalline ceramics, J. Mater. Sci. Mater. Electron. 1 (2014) 2341–2348.
[32] A. Ubaldini, V. Buscaglia, C. Uliana, G. Costa, M. Ferretti, Kinetics and mechanism of formation of barium zirconate from barium carbonate and zirconia powders, J. Am. Ceram. Soc. 86 (1) (2003) 19–25, https://doi.org/10.1111/j.1151-2916.2003.tb03271.x.
[33] Y. Sun, et al., Preparation modification and water resistance optimization of Cu-Mn CO catalyst, Appl. Surf. Sci. 708 (Nov. 2025) 163768, https://doi.org/10.1016/j.apsusc.2025.163768.
[34] J. Liu, W. Lv, Y. Mou, C. Chen, Y. Kang, Coalescence behavior of Cu nanoparticles during sintering: based on atomic scale to macro scale, J. Mater. Res. Technol. 27 (Nov. 2023) 2490–2507, https://doi.org/10.1016/j.jmrt.2023.10.080.
[35] S. Katyayan, S. Agrawal, Study of optical behaviour of Eu3+ and Tb3+ doped zirconate perovskite phosphors prepared by molten salt technique, Opt. Quant. Electron. 52 (1) (Dec. 2019) 18, https://doi.org/10.1007/s11082-019-2129-9.
[36] P. Manju, M.R. Ajith, D. Jaiswal-Nagar, Synthesis and characterization of BaZrO3 nanoparticles by citrate-nitrate sol-gel auto-combustion technique: systematic study for the formation of dense BaZrO3 ceramics, J. Eur. Ceram. Soc. 39 (13) (Oct. 2019) 3756–3767, https://doi.org/10.1016/j.jeurceramsoc.2019.03.048.
[37] K. Selvakumar, S. Rajendran, M. Ramesh Prabhu, Influence of barium zirconate on SPEEK-based polymer electrolytes for PEM fuel cell applications, Ionics 25 (5) (May 2019) 2243–2253, https://doi.org/10.1007/s11581-018-2613-4.
[38] H.M. Altass, A.E.R.S. Khder, Surface and catalytic properties of triflic acid supported zirconia: effect of zirconia tetragonal phase, J. Mol. Catal. Chem. 411 (Jan. 2016) 138–145, https://doi.org/10.1016/j.molcata.2015.10.022.
[39] M.A. Ansari, N. Jahan, Structural and optical properties of BaO nanoparticles synthesized by facile Co-precipitation method, Mater. Highlights 2 (1–2) (Mar. 2021) 23–28, https://doi.org/10.2991/mathi.k.210226.001.
[40] D.F. Cañon-Davila, A.M. Castillo-Paz, S.M. Londoño-Restrepo, H. Pfeiffer, R. Ramirez-Bon, M.E. Rodriguez-Garcia, Study of the coalescence phenomena in biogenic nano-hydroxyapatite produced by controlled calcination processes at low temperature, Ceram. Int. 49 (11) (June 2023) 17524–17533, https://doi.org/10.1016/j.ceramint.2023.02.119. Part A.
[41] K.-N. Chen, C.-M. Hsu, J. Liu, Y.-T. Chiu, C.-F. Yang, Effect of different heating process on the photoluminescence properties of perovskite Eu-Doped BaZrO3 powder, Appl. Sci. 6 (1) (Jan. 2016), https://doi.org/10.3390/app6010022. Art. no. 1.
[42] S. Bagyalakshmi, M. Subash, R. Uthrakumar, S. Aravindan, and K. Kaviyarasu, "Highly absorption and an excellent optical bandgap of CuO doped Fe nanoparticles for advanced photocatalytic applications. | EBSCOhost." Accessed: May 14, 2025. Available: https://openurl.ebsco.com/contentitem/doi:10.152512FDJNB.2024.191.201?sid=ebsco:plink:crawler&id=ebsco:doi:10.152512FDJNB.2024.191.201.
[43] E.C. Aguiar, A.Z. Simões, C.A. Paskocimas, M. Cilense, E. Longo, J.A. Varela, Photoluminescence of BaZrO3 explained by a order/disorded transformation, J. Mater. Sci. Mater. Electron. 26 (4) (Apr. 2015) 1993–2001, https://doi.org/10.1007/s10854-015-2701-4.
[44] Kiyoshi Kanie, Yuki Seino, Masaki Matsubara, Masafumi Nakaya, Hydrothermal synthesis of BaZrO3 fine particles controlled in size and shape and fluorescence behavior by europium doping | request PDF, New J. Chem. 38 (8) (July 2014) 3548–3555, https://doi.org/10.1039/C4NJ00443D.
[45] M. Thommes, et al., Physisorption of gases, with special reference to the evaluation of surface area and pore size distribution (IUPAC technical report), Pure Appl. Chem. 87 (9–10) (Oct. 2015) 1051–1069, https://doi.org/10.1515/pac-2014-1117.
[46] A. Gnanasekar, P. Gurusamy, G. Deivasigamani, Investigation of structural, optical, and frequency-dependent dielectric properties of barium zirconate (BaZrO3) ceramic prepared via wet chemical auto-combustion technique, Eng. Proc. 87 (1) (2025) 1, https://doi.org/10.3390/engproc2025087022.
[47] D.M. Nzilu, E.S. Madivoli, D.S. Makhanu, S.I. Wanakai, G.K. Kiprono, P.G. Kareru, Green synthesis of copper oxide nanoparticles and its efficiency in degradation of rifampicin antibiotic, Sci. Rep. 13 (1) (Aug. 2023) 14030, https://doi.org/10.1038/s41598-023-41119-z.
[48] S.B. Jathar, et al., Ternary Cu2SnS3: synthesis, structure, photoelectrochemical activity, and heterojunction band offset and alignment, Chem. Mater. 33 (6) (Mar. 2021) 1983–1993, https://doi.org/10.1021/acs.chemmater.0c03223.
[49] R.E. Aderne, et al., On the energy gap determination of organic optoelectronic materials: the case of porphyrin derivatives, Mater. Adv. 3 (3) (Feb. 2022) 1791–1803, https://doi.org/10.1039/D1MA00652E.
[50] G.K. Gupta, A. Garg, A. Dixit, Electrical and impedance spectroscopy analysis of sol-gel derived spin coated Cu2ZnSnS4 solar cell, J. Appl. Phys. 123 (1) (Jan. 2018), https://doi.org/10.1063/1.5002619.
[51] X. Wei, et al., Realization of BaZrS3 chalcogenide perovskite thin films for optoelectronics, Nano Energy 68 (Feb. 2020) 104317, https://doi.org/10.1016/j.nanoen.2019.104317.
[52] G. Cabello, et al., Photochemical synthesis of AZrO3−X thin films (A=Ba, Ca and Sr) and their characterization, Ceram. Int. 40 (6) (July 2014) 7761–7768, https://doi.org/10.1016/j.ceramint.2013.12.118.
[53] L. Wang, et al., Highly selective catalytic oxidation of methane to methanol using Cu–Pd/anatase, Energy Environ. Sci. 17 (23) (Nov. 2024) 9122–9133, https://doi.org/10.1039/D4EE02671C.
[54] M.C. Biesinger, Advanced analysis of copper X-ray photoelectron spectra, Surf. Interface Anal. 49 (13) (2017) 1325–1334, https://doi.org/10.1002/sia.6239.
[55] Y. Gao, B. Feng, L. Miao, Y. Chen, J. Di, Determination of Cr(III) ions based on plasmonic sensing and anodic stripping voltammetry with amplification of Ag nanoparticles, Microchem. J. 157 (Sept. 2020) 104995, https://doi.org/10.1016/j.microc.2020.104995.
[56] M.S. Hammer, D. Rauh, V. Lorrmann, C. Deibel, V. Dyakonov, Effect of doping- and field-induced charge carrier density on the electron transport in nanocrystalline ZnO, Nanotechnology 19 (48) (Dec. 2008) 485701, https://doi.org/10.1088/0957-4484/19/48/485701.
[57] Y. Wang, W. Duan, B. Liu, X. Chen, F. Yang, J. Guo, The effects of doping copper and mesoporous structure on photocatalytic properties of TiO2, J. Nanomater. 2014 (1) (2014) 178152, https://doi.org/10.1155/2014/178152.
[58] A.B. Abdeta, et al., Mo-/O-deficient Bi2Mo3(S,O)12 oxysulfide for enhanced visible-light photocatalytic H2 evolution and pollutant reduction via in-situ generated protons: a case of material design in converting an oxidative Bi2Mo3O12 catalyst for the reduction, J. Catal. 413 (Sept. 2022) 1056–1069, https://doi.org/10.1016/j.jcat.2022.08.017.
[59] S. Cao, L. Piao, Considerations for a more accurate evaluation method for photocatalytic water splitting, Angew. Chem. Int. Ed. 59 (42) (2020) 18312–18320, https://doi.org/10.1002/anie.202009633.
[60] V. Shvalagin, et al., Simultaneous photocatalytic production of H2 and acetal from ethanol with quantum efficiency over 73% by protonated poly(heptazine imide) under visible light, ACS Catal. 14 (19) (Sept. 2024) 14836–14854, https://doi.org/10.1021/acscatal.4c04180.
[61] K. Kaiya et al., "Water splitting over transition metal-doped SrTiO3 photocatalysts with response to visible light up to 660 nm," Chem. Sci., vol. 15, no. 39, pp. 16025–16033, doi: 10.1039/d4sc03978e.
[62] Z. Yang, et al., Solid-state, low-cost, and green synthesis and robust photochemical hydrogen evolution performance of ternary TiO2/MgTiO3/C photocatalysts, iScience 14 (Apr. 2019) 15–26, https://doi.org/10.1016/j.isci.2019.03.009.
[63] Y. Fan, J. Hu, T. Li, S. Xu, S. Chen, H. Yin, Enhanced photocatalytic hydrogen evolution through MoS2 quantum dots modification of bismuth-based perovskites, Chem. Commun. 60 (8) (Jan. 2024) 1004–1007, https://doi.org/10.1039/D3CC05781J.
[64] X. Zhao, et al., Perovskite microcrystals with intercalated monolayer MoS2 nanosheets as advanced photocatalyst for solar-powered hydrogen generation, Matter 3 (3) (Sept. 2020) 935–949, https://doi.org/10.1016/j.matt.2020.07.004.
[65] J. Xiao, et al., Enhanced overall water splitting by a zirconium-doped TaON-Based photocatalyst, Angew. Chem. Int. Ed. 61 (17) (2022), https://doi.org/10.1002/anie.202116573 p. e202116573.
[66] H. Li, et al., Zr-doped $BaTaO_2$ N photocatalyst modified with Na–Pt cocatalyst for efficient hydrogen evolution and Z-scheme water splitting, EES Catal 1 (1) (2023) 26–35, https://doi.org/10.1039/D2EY00031H.
[67] S. Nishimae, et al., Active BaTaO 2 N photocatalysts prepared from an amorphous Ta 2 O 5 precursor for overall water splitting under visible light, J. Mater. Chem. A 11 (12) (2023) 6299–6310, https://doi.org/10.1039/D2TA10010J.
[68] X. Chen, et al., Three-dimensional porous g-C3N4 for highly efficient photocatalytic overall water splitting, Nano Energy 59 (May 2019) 644–650, https://doi.org/10.1016/j.nanoen.2019.03.010.
[69] Z. Pan, et al., Photoreduced graphene oxide as a conductive binder to improve the water splitting activity of photocatalyst sheets, Adv. Funct. Mater. 26 (38) (2016) 7011–7019, https://doi.org/10.1002/adfm.201602657.

[70] J. Wu, et al., Breaking through water-splitting bottlenecks over carbon nitride with fluorination, Nat. Commun. 13 (1) (Nov. 2022) 6999, https://doi.org/10.1038/s41467-022-34848-8.
[71] Q. Wu, et al., A molybdenum sulfo-oxide/cobalt oxysulfide Z-scheme heterojunction catalyst for efficient photocatalytic hydrogen production and pollutant reduction, J. Mater. Chem. A 10 (10) (Mar. 2022) 5328–5349, https://doi.org/10.1039/D1TA09053D.
[72] Á. Kmetykó, et al., Photocatalytic H2 Evolution Using Different Commercial TiO2 Catalysts Deposited with Finely Size-Tailored Au Nanoparticles: critical Dependence on Au Particle Size, Materials 7 (12) (Dec. 2014) 7615–7633, https://doi.org/10.3390/ma7127615.
[73] K. Maeda, D. Lu, K. Domen, Solar-driven Z-scheme water splitting using modified BaZrO3–BaTaO2N solid solutions as photocatalysts, ACS Catal. 3 (5) (May 2013) 1026–1033, https://doi.org/10.1021/cs400156m.
[74] J. Li, et al., Biological impact of lead from halide perovskites reveals the risk of introducing a safe threshold, Nat. Commun. 11 (1) (Jan. 2020) 310, https://doi.org/10.1038/s41467-019-13910-y.
[75] B. Wu, et al., Synergistic tuning of heterovalent states and oxygen-vacancy defect engineering in hydrophilic W-Doped Sb2OS2 for enhanced nitrogen photoreduction to ammonia, ACS Appl. Mater. Interfaces 16 (43) (Oct. 2024) 58764–58779, https://doi.org/10.1021/acsami.4c16630.
[76] Y. Yuan, et al., Synthesis and photocatalytic characterization of a new photocatalyst BaZrO3, Int. J. Hydrogen Energy 33 (21) (Nov. 2008) 5941–5946, https://doi.org/10.1016/j.ijhydene.2008.07.052.